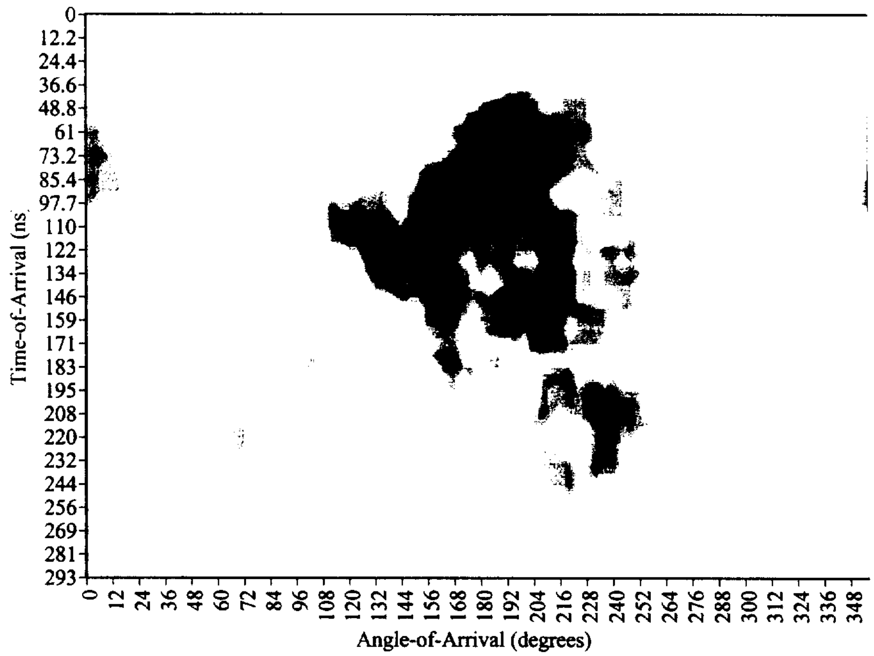

Figure 6-35: Cluster map at location B

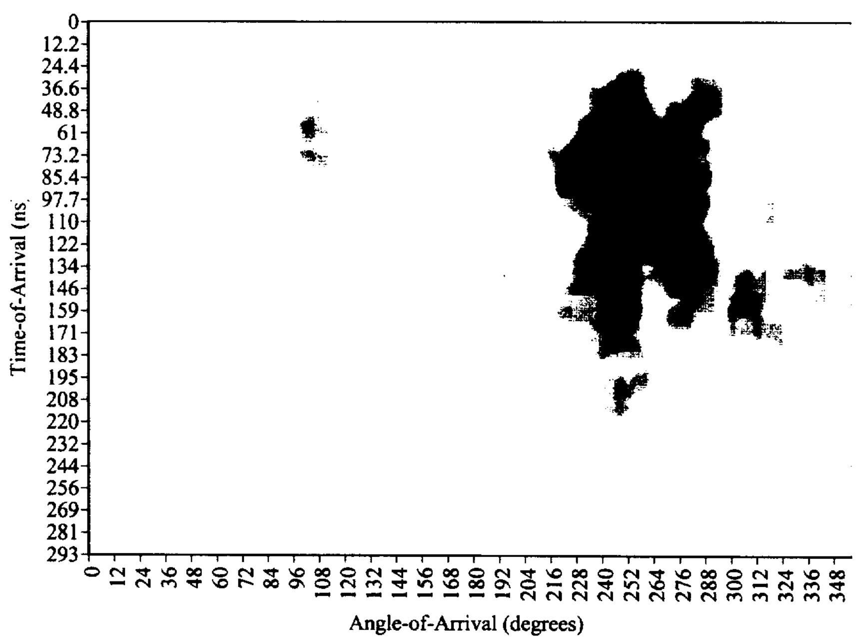

Figure 6-36: Cluster map at location M

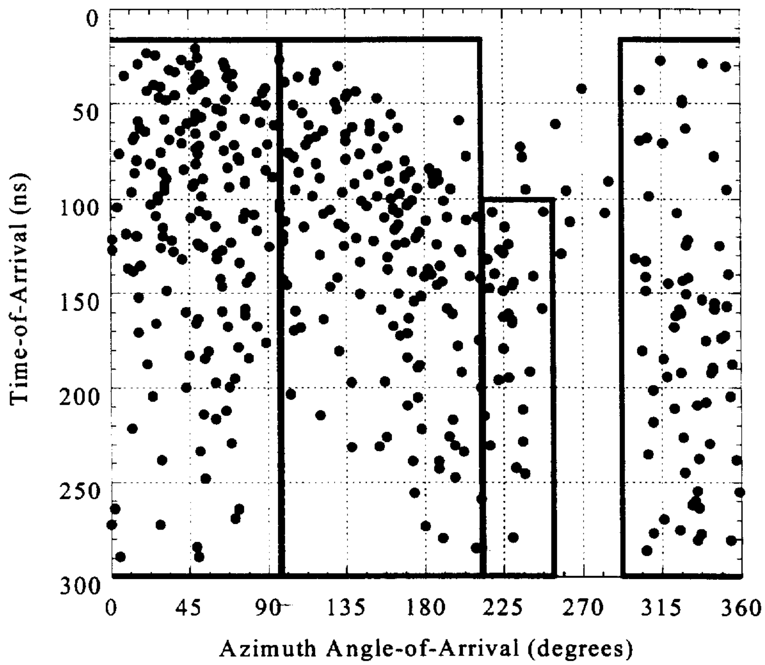

Figure 6-37: Cluster regions selected for recovered signals at location P.

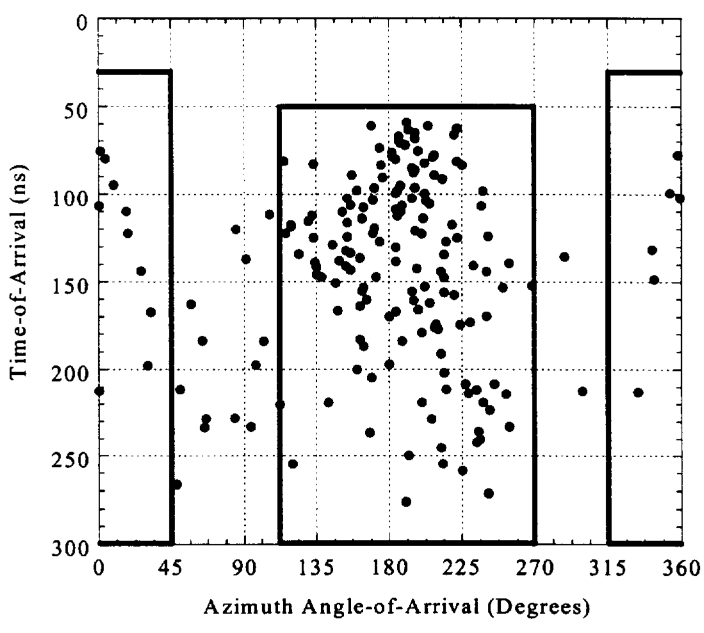

Figure 6-38: Cluster regions selected for recovered signals at location B.

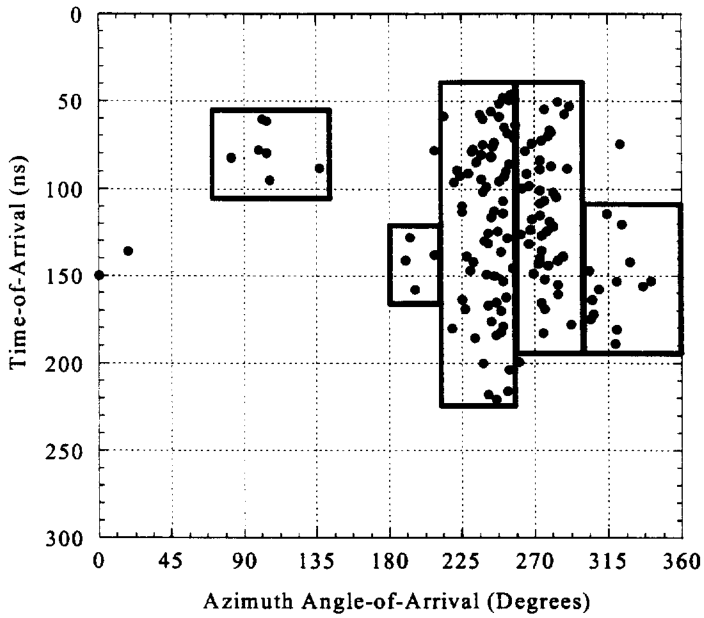

Figure 6-39: Cluster regions selected for recovered signals at location M.

of signals is also reported relative to the energy in the first arrival in the first cluster, which is normalized to 1, and is referred to as the normalized relative energy, as in [49].

With the measurements at locations A and E excluded again, due to the low SNR, the resulting UWB cluster energy versus relative delay models for the indoor channel are shown below in Figure 6-40 and Figure 6-41. The first plot reports the decay of the energy in the recovered waveforms, and the second reports the energy as a function of the recovered amplitude only, under the assumption that all incident waveforms are identical. Several values for the decay exponent Γ are shown for each plot, in order to demonstrate the consistency of the results. Γ_{med} is the median and Γ_{mean} represents the mean of the values obtained by considering the best-fit line for each measurement location individually. Γ_{LS} is the exponent of the best fit line obtained by considering the clusters from all measurement locations simultaneously. In both cases, the results are fairly close, and Γ_{LS} is reported as the rate of decay of the inter-cluster energy versus delay. These results compare to values of 33.6 ns and 78.0 ns reported in [49] for two different buildings, and 60 ns reported in [37]. Thus the UWB signals recovered in this case exhibit a rate of decay that is comparable to some of the results reported previously, although it has

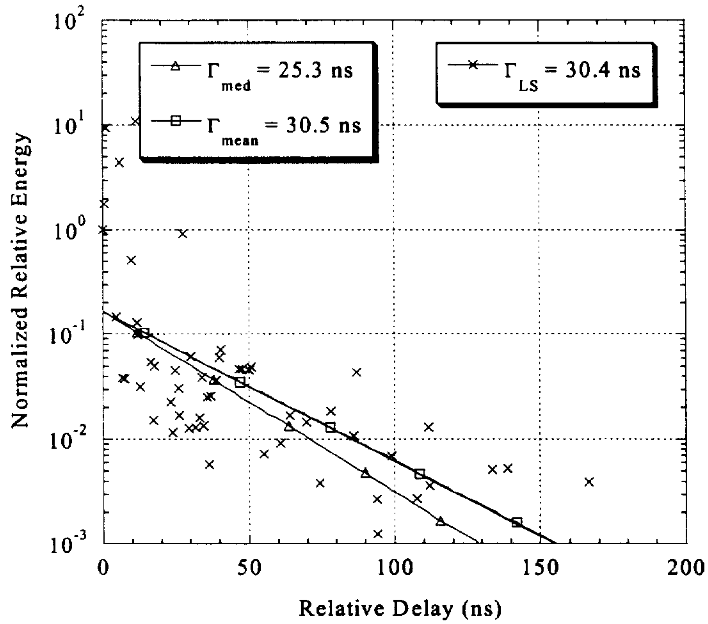

Figure 6-40: Inter-cluster loss vs. relative delay when considering the recovered energy (energy in the first arrival within a cluster).

been noted that this parameter is a strong function of the building architecture, as are many parameters of the propagation channel.

These results allow for comparison against other experiments reported in the literature and for the derivation of a common parameter, the decay exponent, Γ. A non-linear (on a log scale) fit to the data can also be attempted here, in order to obtain a model which weights the strong arrivals early in time more heavily, although there is no readily available basis for comparison in the literature. This is shown for the recovered signal energy in Figure 6-42, with the parameters of the curve fit given in the plot. Although the corresponding plot using the recovered signal amplitudes is not given, it is hypothesized that it would yield similar results, based on the similar values for decay exponents above.

Consider next the intra-cluster rate of decay, or the rate at which the recovered energy in the signal arrivals within a cluster falls off as a function of the delay. Following the terminology of [37] and [49], this is also called the ray decay rate. These plots are shown below in Figure 6-43 and Figure 6-44. The absolute deviation between the mean and median of the results from

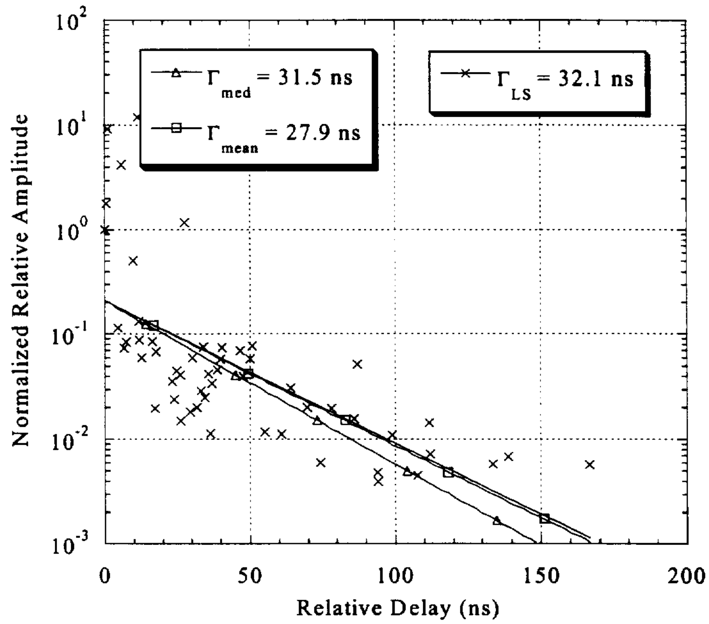

Figure 6-41: Inter-cluster loss vs. relative delay when considering the amplitude of the recovered waveform (amplitude of first arrival within a cluster).

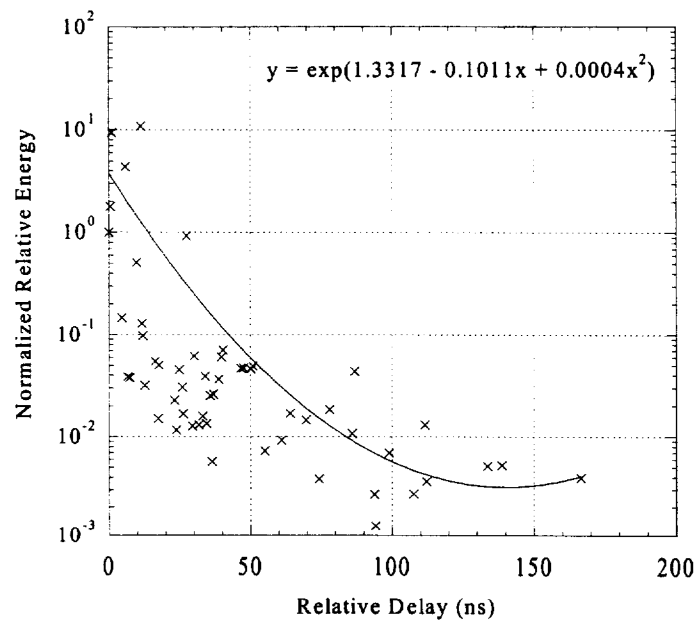

Figure 6-42: Nonlinear (on a log scale) fit to inter-cluster loss vs. relative delay when considering the recovered energy.

each measurement location and the least-squares fit to all of the recovered signal information is larger here, excluding the results at locations A and E. The results generated by considering the energy in the recovered waveform and the results from the amplitude only are very close. In [49], very different results are found for the inter-cluster decay exponent γ, depending on which building the measurements were conducted in. In one building, a value of 28.6 ns is reported for γ, while in another building γ is found to be 82.2 ns. The earlier reference, [37] reported a γ of 20 ns. It is noted in [49] that the first measurement was made in a building constructed primarily out of cinder blocks, while the second was made in a building constructed from a steel-frame and gypsum boards. This difference in construction is reflected in the different rates of decay. The values for γ derived here for the UWB propagation channel are in the same neighborhood as those reported for the steel-frame building in [49].

Further, considering the relationship between Γ and γ, in both sets of measurements reported in [49] the values for Γ and γ are fairly close. In one case Γ is larger than γ, while in the other the opposite is true. What is not indicated in the paper is the physical relationship between the transmitter and the receiver. The results obtained here can be explained for the transmitter and receiver relationships at which the measurements were made. This relation is shown for all cases in Figure 6-1, and it can be seen that with the exception of the measurements at locations F1 and F2, at least one wall separates the transmitter and the receiver. Each cluster then represents a path that exists between the transmitter and the receiver along which signals propagate. This cluster path is generally a function of the architecture of the building itself, while the arrivals within a cluster are due to secondary reflections off of furniture or other objects. The implications are that the primary source of degradation is in the propagation from the transmit antenna to the receive antenna through the features of the building. This captured in the decay exponent Γ. Secondary reflections off of other objects in the neighborhood of the receive antenna do not always involve the penetration of additional obstructions, and therefore tend to contribute less to the decay of the signals. This is likely due to the building architecture and perhaps to the propagation characteristics of the UWB waveforms. This property of the UWB waveforms probably merits further study in different buildings.

As discussed in [49] and [37], a Rayleigh distribution has been shown to provide a good fit to the deviation of the arrival energy from the mean curve, where the Rayleigh probability

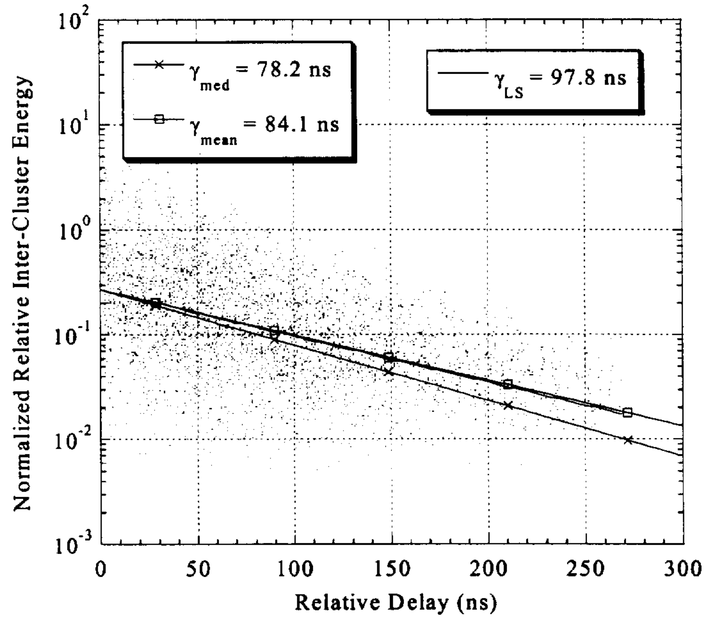

Figure 6-43: Intra-cluster loss versus delay energy.

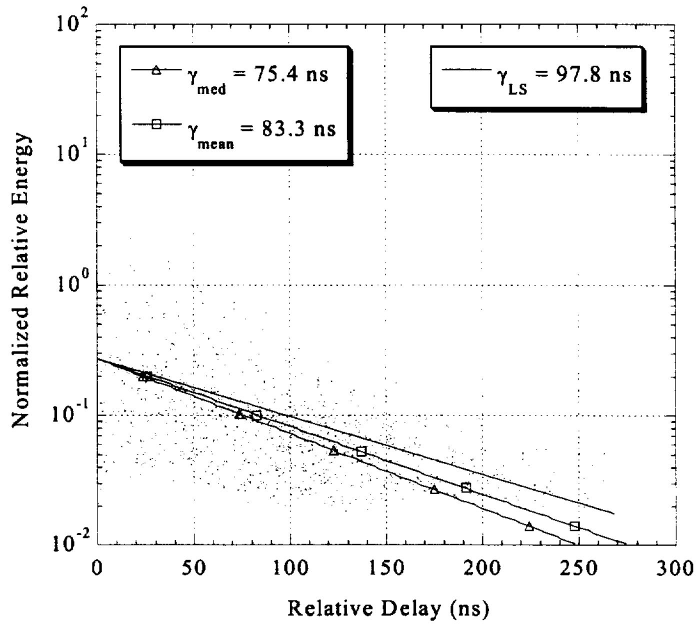

Figure 6-44: Intra-cluster loss vs. delay amplitude

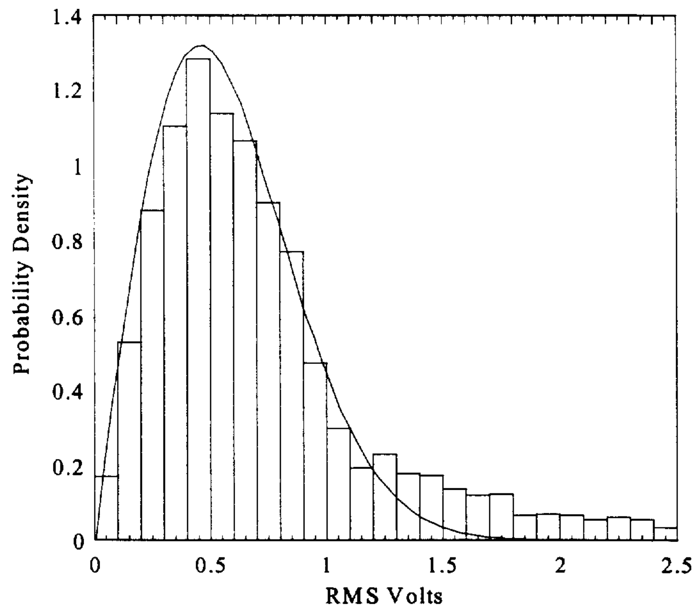

Figure 6-45: Distribution of the arrival energy deviation from the mean, with a Rayleigh density overlayed.

density function is given by

$$f_x(x) = \frac{x}{\alpha^2} e^{-\frac{x^2}{2\alpha^2}}$$

A histogram of the deviation values is shown in Figure 6-45 and 6-46, with a Rayleigh density with $\alpha = 0.46$ overlaid on top of the recovered distribution. This distribution represents the best-fit to the recovered UWB data when considering the Rayleigh, lognormal, Nakagami-m and Rician distributions.

Consider next the angle-of-arrival properties of the cluster model. Assuming again the separable impulse response of equation (6.6), the model proposed in [49] to describe the angular impulse response is

$$h(\theta) = \sum_{l=0}^{\infty} \sum_{k=0}^{\infty} \beta_{kl} \delta (\theta - \Theta_l - \omega_{kl}) \tag{6.7}$$

where β_{kl} is the amplitude of the k^{th} arrival in the l^{th} cluster, Θ_l is the mean azimuth angle-

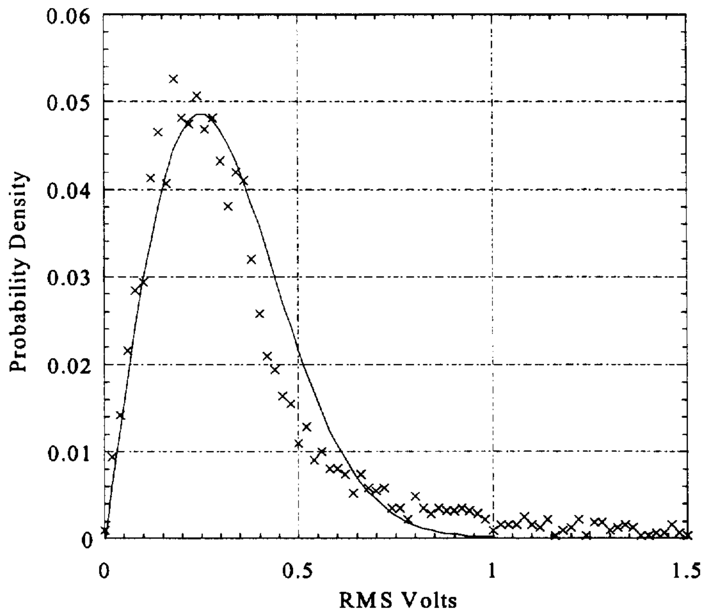

Figure 6-46: Histogram of the arrival energy deviation from the mean, with a Rayleigh density overlayed.

of-arrival of the l^{th} cluster and ω_{kl} is the azimuth angle-of -arrival of the k^{th} arrival in the l^{th} cluster, relative to Θ_l. It is proposed in [49] that Θ_l is distributed uniformly in angle, and ω_{kl} is distributed according to a zero-mean Laplacian distribution,

$$p(\theta) = \frac{1}{\sqrt{2}\sigma} e^{-\left|\sqrt{2}\theta/\sigma\right|} \tag{6.8}$$

The recovered ray or intra-cluster arrivals were tested against Gaussian and Laplacian hypotheses, and the best fit distribution and resulting standard deviation were reported. It was determined that the recovered UWB signals were best fit to a Laplacian density, with a standard deviation, σ, of 38^o. The recovered signal information and the best-fit distribution are shown in Figure 6-47 at $1^o$of resolution, and in Figure 6-48 at five degrees of resolution. Note that these are histograms, and only take into account the fact that a signal has arrived, but not the energy in the arrival. The angular distributions associated with the waveform energy and amplitude are therefore identical. These distributions compare with standard deviations on the Laplacian density of $25.5^o$and 21.5^oreported in [49] as the best fit to the recovered angular information for

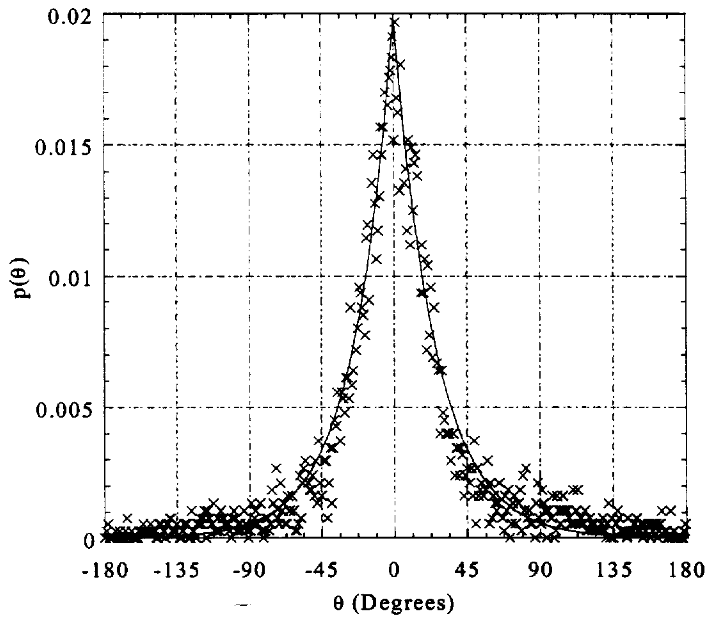

Figure 6-47: Ray arrival angles at 1°of resolution and a best fit Laplacian density with σ=38°

two different buildings. It is likely that this parameter is a function of the building architecture, which again would suggest that further propagation studies are needed to determine whether the results presented here are typical. It is also possible that the difference in the results is due in part to the fractional bandwidth of the UWB waveforms used in this study. The penetration properties of these signals, including the larger γ, might lead to the detection of responses that would remain undetected at if transmitted at a single frequency or over a smaller frequency range.

It was found in [49] that the relative cluster azimuth arrival angles were approximated by a uniform distribution over all angles. The recovered cluster angles in this work are shown in Figure 6-49, relative to the reference cluster angle-of-arrival, where the reference cluster is taken to be the first cluster to arrive in time, for each measurement location. This distribution is also approximately uniform, although it is noted that no clusters were reported to exist at angles above approximately 135°. It is conjectured that if more measurements were taken, angles would occur in this region, and this function would tend to more closely approximate a uniform distribution.

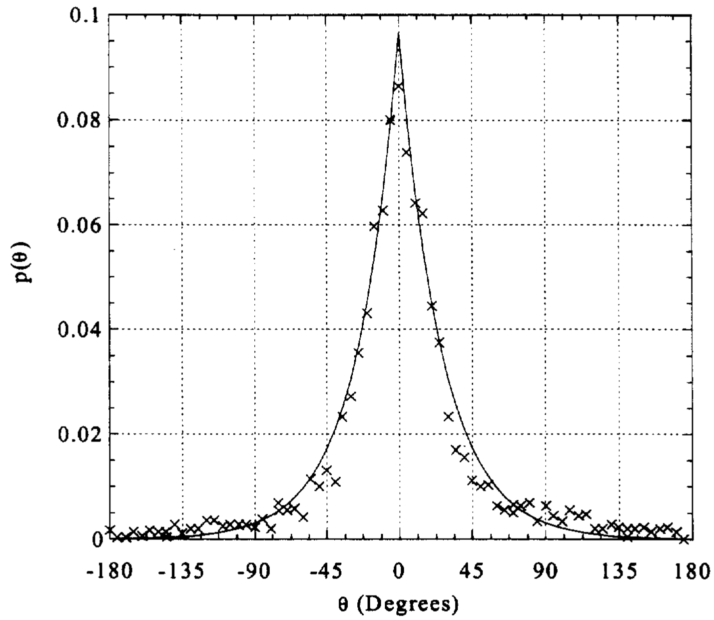

Figure 6-48: Ray arrival angles at 5°of resolution and a best fit Laplacian density with σ=37°

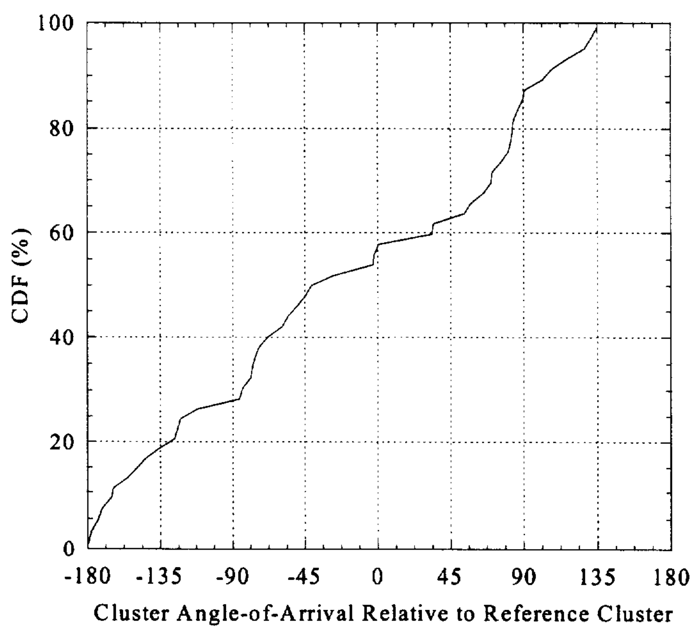

Figure 6-49: Distribution of the cluster azimuth angle-of-arrival, relative to the reference cluster.

Finally, in order to complete this model of the UWB propagation channel, based on the multipath clustering phenomenon, the rate of the cluster and the ray arrivals must be determined. Again following the model presented in [49], the inter-arrival times are hypothesized to follow an exponential rate law, given as

$$p(T_l|T_{l-1}) = \Lambda e^{-\Lambda(T_l - T_{l-1})} \tag{6.9}$$

$$p(\tau_{kl}|\tau_{k-1,l}) = \lambda e^{-\lambda(T_l - T_{l-1})} \tag{6.10}$$

where Λ is the cluster arrival rate and λ is the ray arrival rate. Following this model, the best fit exponential distributions, parameterized on Λ and λ were determined for the recovered UWB cluster and ray arrival times, respectively. The resulting plots are shown in Figure 6-50 and Figure 6-51. The ray arrival rate determined for the UWB signals was faster than that reported in either [49] or [37]. A ray arrival rate of $1/\lambda$=2.3 ns defined the best-fit exponential distribution for the ray arrival times over all measurement locations, while ray arrival rates of $1/\lambda$=5.1 ns and $1/\lambda$=6.6 ns were reported in [49] for the two different buildings. A ray arrival rate of $1/\lambda$=5.0 ns was given in [37]. Several reasons are possible for the faster arrival rate. First, it is again probably due at least in part to the building architecture. Second, the fractional bandwidth of the UWB signals and the post-processing algorithms permit multipath time resolution on the order of 1 ns. The measurement equipment used in [49] allowed a time resolution on the incident signals of about 3 ns. Also shown in Figure 6-50 is a curve which represents the best-fit exponential to ray arrival times of greater than 8 ns, although this represents less than 10% of the values.

A cluster arrival rate of $1/\Lambda$=45.5 ns was found to define the best-fit exponential distribution in the UWB signal propagation model. This value is larger than the cluster arrival rates of 16.8 ns and 17.3 ns reported in [49], but less than the 300 ns given in [37]. Again, several explanations are possible to describe the differences. It could be due to the difference in the fractional bandwidths of the signals involved, the sensitivity of the measurement equipment or the building architecture. As discussed above, it could also be due to the orientation of the transmitter and receiver in the building. This information is not given in [48] or [49], but for the 14 measurement locations used in this work, only two were taken in the same room, and in

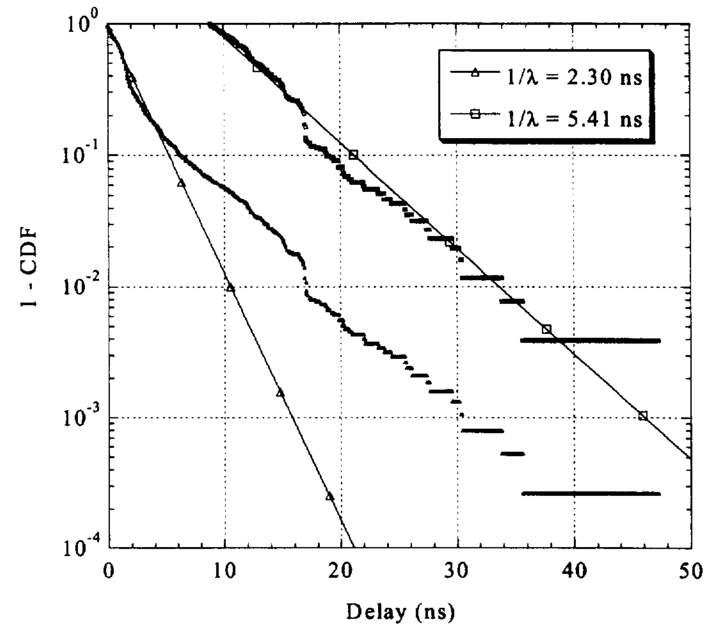

Figure 6-50: Ray arrival rate for the indoor UWB channel considered here.

Parameter	UWB Propagation	Spencer et al.	Spencer et al.	Saleh-Valenzuela
Γ	27.9 ns	33.6 ns	78.0 ns	60 ns
γ	84.1 ns	28.6 ns	82.2 ns	20 ns
$1/\Lambda$	45.5 ns	16.8 ns	17.3 ns	300 ns
$1/\lambda$	2.3 ns	5.1 ns	6.6 ns	5 ns
σ	37°	25.5°	21.5°	-

Table 6.2: Summary of propagation model parameters

the rest, the transmitter and receiver were separated by at least one wall. As shown in Table 6.1, eight out of the ten sets of measurements involved a separation between the transmitter and receiver of greater than 10 meters. At this separation, it is possible that relatively few distinct paths between the transmitter and receiver, each corresponding to a cluster, exist, as compared with the measurements in [48], [49]. Without further knowledge of the measurement scenario in [48] and [49], it is impossible to draw more concrete explanations.

The model parameters derived herein for the UWB signal propagation model and a comparison with the earlier work in [48], [49], [37] are summarized in Table 6.2.

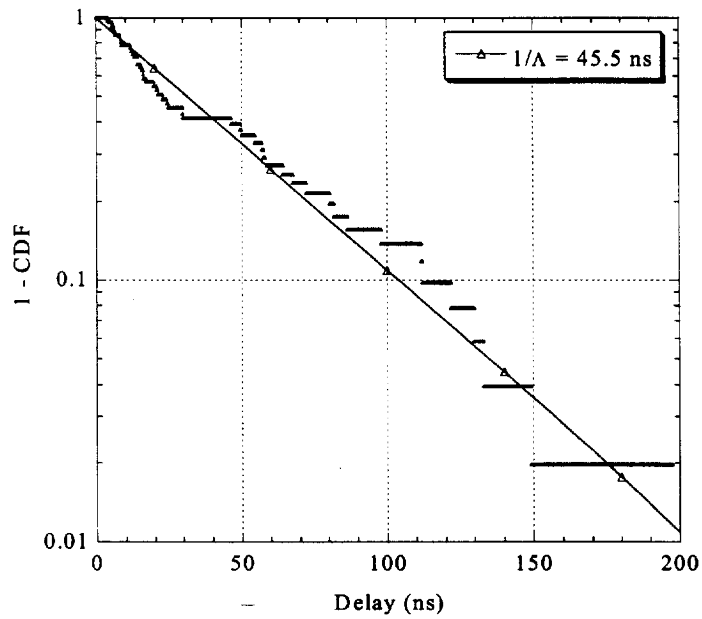

Figure 6-51: Cluster arrival rate for the indoor UWB channel considered here.

6.3 Additional Models for the Ultra-Wideband Propagation Channel

A characterization of the UWB propagation channel can also be developed without considering cluster information. In this case, it is of interest to calculate the spatio-temporal distribution of the received UWB signals and to examine any correlation between the time-of-arrival and angle-of-arrival of the received UWB signals. First, channel models will be discussed which consider the spatial and temporal variations in the channel independently, then joint spatio-temporal distributions will be presented.

6.3.1 Independent spatial and temporal channel descriptions - best-fit distributions

Communication channels are often characterized by assuming that the spatial and temporal variations in the channel are independent [35], [49]. Under this assumption, consider the best-fit distributions to the recovered angles-of-arrival and the recovered energy of all signals, shown in Figures 6-52, 6-53 and 6-54. Two versions of the angle-of-arrival distribution are shown, with markedly different results. For the angle-of-arrival distributions, each plot represents the best-fit distribution which results when the data is fit to a Laplacian distribution and to a Gaussian distribution. In both cases here, as in [49], the Laplacian distribution provides the best description of the angle-of-arrival information. An intuitive explanation for the suitability of the Laplacian distribution in the indoor environment is that deviations in the propagation path from the line-of-sight (LOS) path will often result in a path with greater attenuation than the LOS path. Thus more signals are detected at arrival angles close to the LOS arrival angle, which gives rise to the distinct peak in the density function. In 6-52, all signals are weighted equally in the distribution, regardless of the recovered energy, while in 6-53, each signal contributes a weight to the distribution proportional to the recovered energy. The implication here again is that for these measurements, large signals tend to arrive at small deviations from the LOS path arrival angle. This result will explored in greater detail below. Figure 6-54 shows the best fit lognormal distribution to the recovered signal energies. In this case, a lognormal, a Nakagami and a Rayleigh distribution were fit to the data, and the lognormal distribution was retained as the one with the lowest mean-squared error. Intuition here follows the theory of lognormal fading in a shadowed environment [36]. Representing the lognormal distribution as

$$f_x(x) = \frac{1}{\sigma x\sqrt{2\pi}} e^{-(\ln x - \eta)^2/2\sigma^2} \tag{6.11}$$

the best-fit parameters of the lognormal distribution were found to be σ =1.93 and $\eta = 0$. In each case, the distributions are normalized to yield a total probability mass of 1. These distributions give a rough idea of the statistical properties of the channel, in the absence of any cluster information or correlation between the spatial and temporal distributions.

6.3.2 Independent spatial and temporal channel descriptions - moments

Typical parameters by which the temporal and spatial distributions of signal energy are measured include the first moment and the root of the second moment of the power delay profile. These moments are defined here under the assumptions of discrete time signals and a specular multipath model. The temporal variations are described by the first and root of the second

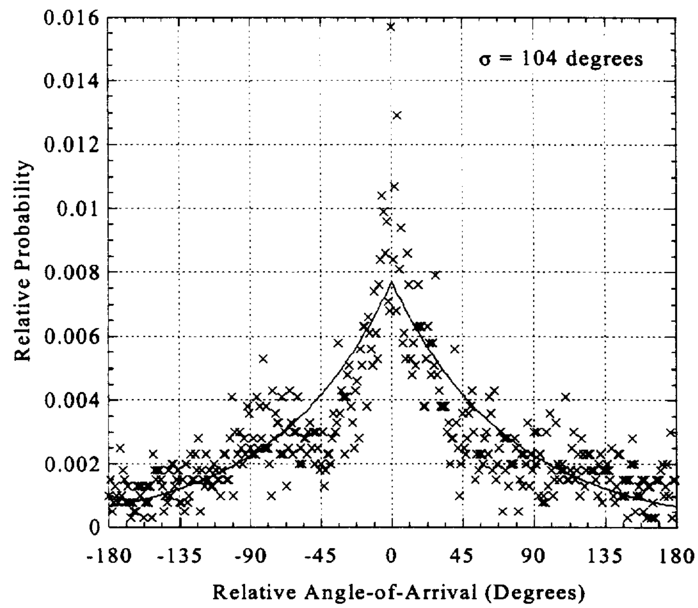

Figure 6-52: Best fit Laplacian distribution to the recovered angles from all measurement locations, with a resolution of 1^o. All signals are weighted equally in the distribution.

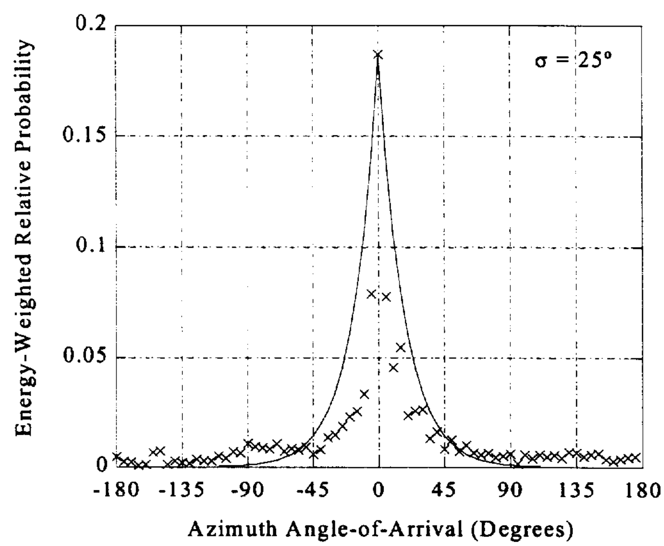

Figure 6-53: Best fit Laplacian distribution to the recovered angles from all measurement locations, with a resolution of 5^o. All signals are weighted in the distribution according to the recovered energy.

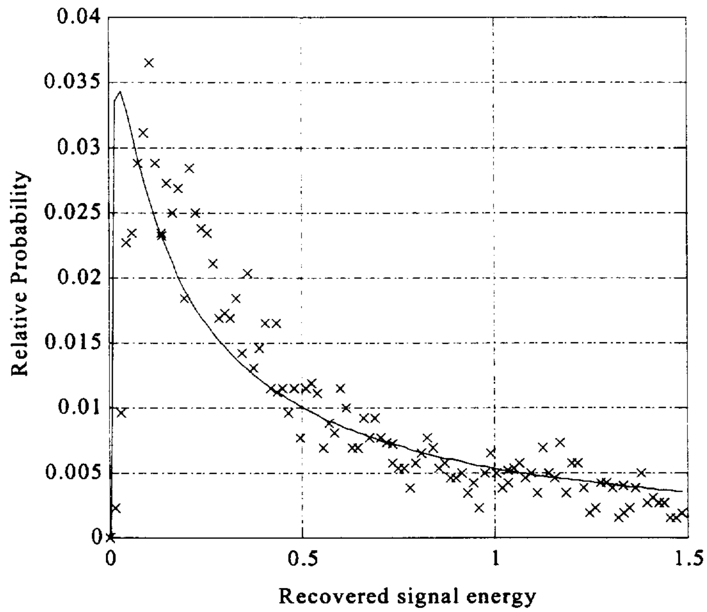

Figure 6-54: Best fit lognormal distribution to the recovered signal energy from all measurement locations except A and E, with $\sigma = 1.93$ and $\eta = 0$. Energy is calculated from the recovered waveforms.

moment of the power delay profile as

$$\overline{T} = \frac{\sum_{k=0}^{K-1} \sum_{n=0}^{N-1} (nT_s)\, \beta_{n,k}^2}{\sum_{k=0}^{K-1} \sum_{n=0}^{N-1} \beta_{n,k}^2} \tag{6.12}$$

$$\sigma_T = \sqrt{\frac{\sum_{k=0}^{K-1} \sum_{n=0}^{N-1} \left(nT_s - \overline{T}\right)^2 \beta_{n,k}^2}{\sum_{k=0}^{K-1} \sum_{n=0}^{N-1} \beta_{n,k}^2}} \tag{6.13}$$

where T_S is the sampling rate, N is the number of time samples considered in the calculation, and K represents the angular samples. $\overline{T}$ is called the power-weighted average time-of-arrival (TOA) and σ_T is known as the delay spread. Assuming that these moments are calculated without regard to the angle-of-incidence, the summation over K removes any dependence on angle from the results.

The spatial distribution of the signal energy can be measured by the first moment and root of the second moment of the received angular profile according to [30]

$$\overline{\phi} = \frac{\sum_{n=N_1}^{N_2-1} \sum_{k=0}^{K-1} \phi_k \beta_{n,k}^2}{\sum_{n=N_1}^{N_2-1} \sum_{k=0}^{K-1} \beta_{n,k}^2} \tag{6.14}$$

$$\sigma_\phi = \sqrt{\frac{\sum_{n=N_1}^{N_2-1} \sum_{k=0}^{K-1} \left(\phi_k - \overline{\phi}\right)^2 \beta_{n,k}^2}{\sum_{n=N_1}^{N_2-1} \sum_{k=0}^{K-1} \beta_{n,k}^2}} \tag{6.15}$$

where ϕ_k represents the k^{th} angle considered in the calculation and n again is a time index. Equation 6.14 is referred to as the power-weighted average AOA, and equation 6.15 is called the rms angle-of-arrival (AOA) or angular spread.

In a narrowband context $\beta_{n,k}$ is the amplitude of the signal component incident at time n from angle k, and $\beta_{n,k}^2$ is then proportional to the incident signal power of this component. In the UWB case, if an assumption is made that all incident waveforms have the same shape, then $\beta_{n,k}$ is the amplitude of a signal incident from angle k at time sample n, and the energy in each pulse cancels between the numerator and the denominator. If the incident pulses are allowed to vary in shape in the calculations, then let $\beta_{n,k}^2$ represent the actual energy in the incident signal, calculated from the recovered waveform. The AOA and TOA statistics for both cases are summarized in Table 6.3 and Table 6.4. In these tables, $\overline{T}_a$ represents the absolute power-weighted average TOA, calculated without regard for the time-of-arrival of the LOS path signal. The symbol $\overline{T}_r$ represents a power- weighted average TOA which is calculated relative to the time-of-arrival of the LOS path signal. The resulting delay spread is the same in both cases.

Note that the angular spread is generally defined over some time window, given in the equation above as $[N_1, N_2 - 1]$. These results are reported for a single time interval which encompasses the entire measurement period in Figure 6-55, and for time intervals of 10 ns, in order to investigate variations in the channel statistics, in Figure 6-56 and Figure 6-57.

Figure 6-55 shows the power-weighted average AOA and the rms AOA, relative to the LOS path AOA, for the signals recovered at each measurement location, where the calculations are performed over the entire 300 ns window. In each plot, the results under an assumption of a static incident waveform and the results if the energy is derived from the individual recovered waveforms are shown. In general, the results corresponding to the two different calculations are close, which gives some validation to the assumption of a static incident pulse shape. These results are summarized in Table 6.3 and Table 6.4, where the median values are also reported. Figure 6-56 shows the cumulative distribution function (CDF) of the calculated angular spreads. This compares with a figure in [29] for outdoor measurements, and the values calculated here are smaller than those in the reference, which is to be expected given that these measurements were made indoors.

The time delay spread is shown as a function of the measurement location in Figure 6-58. These results are catalogued in Table 6.3 and Table 6.4. Considering the results in Table 6.3, where the statistics are calculated without regard to the recovered waveform, the median power-weighted average TOA is given as $\overline{T}_{med} = 87.81$ ns in the absolute case and $\overline{T}_{med} = 51.98$ ns when calculated relative to the arrival time of the LOS path. For Table 6.4, the corresponding numbers are $\overline{T}_{med} = 89.51$ ns and $\overline{T}_{med} = 48.79$ ns. These averages are often not given in channel models, but the rms TOA is a commonly reported channel statistic. The result based on the recovered amplitudes only is $\sigma_T = 45.38$ ns, and $\sigma_T = 45.59$ ns is found when the energy in each recovered waveform is calculated. These numbers compare with median rms delay spreads of 25-50 ns reported in one set of indoor narrowband propagation measurements in an office building at 1.5 GHz [37], and 50-150 ns reported in another [35]. The worst case reported in Table 6.3 is $\sigma_T = 58.46$ ns and the standard deviation on the rms delay spread is 6.79 ns. In Table 6.4, the worst case is $\sigma_T = 54.88$ ns and the standard deviation of the rms delay spread is 6.68 ns. These results compare with worst case RMS delay spreads of 100-200 ns reported in another experiment [35]. The cumulative distribution function of the calculated angle spread numbers are shown in Figure 6-57.

From Table 6.3, Table 6.4 and the discussion above, it is seen that although there appears to be a rough correlation between the parameters and the SNR, as defined in equation 5.1, or propagation distance, the strongest dependence is on the geometry of the situation. This is similar to the narrowband case [30] and makes the properties difficult to predict without taking into account the floor plans.

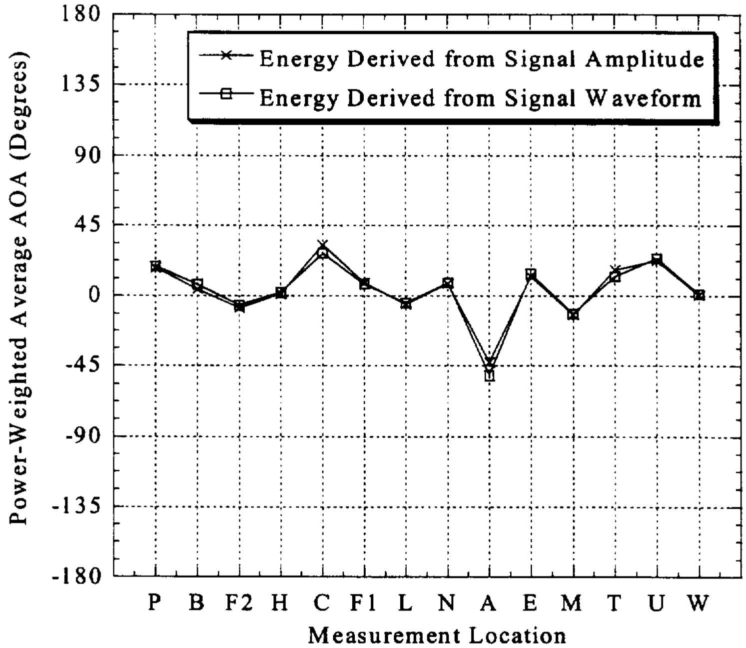

(a)

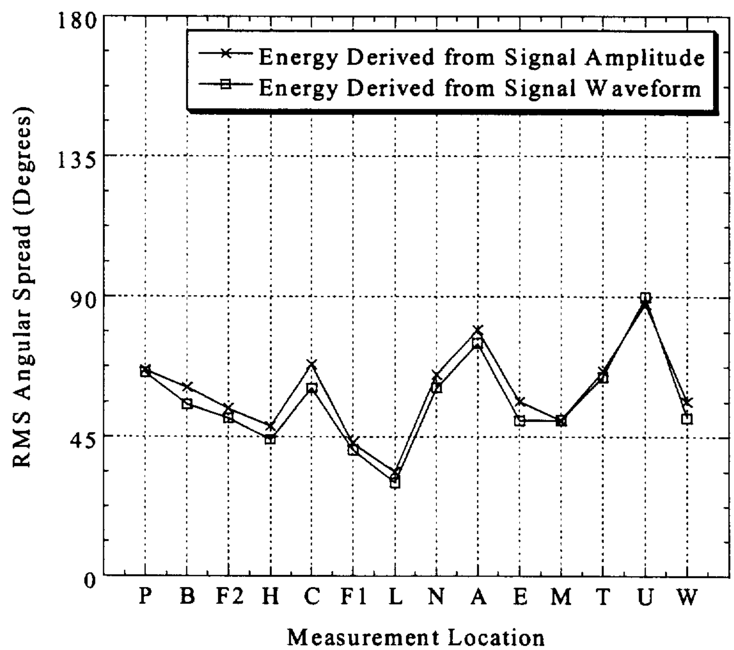

(b)

Figure 6-55: Power-weighted average AOA and rms angular spread for each measurement location. Calculations are reported relative to LOS path arrival angle.

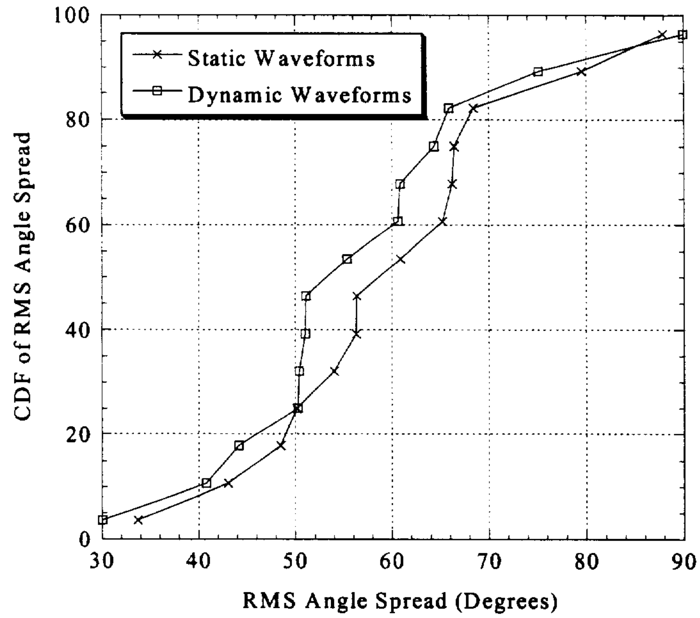

Figure 6-56: CDF of RMS angular spread, calculated over 300 ns window.

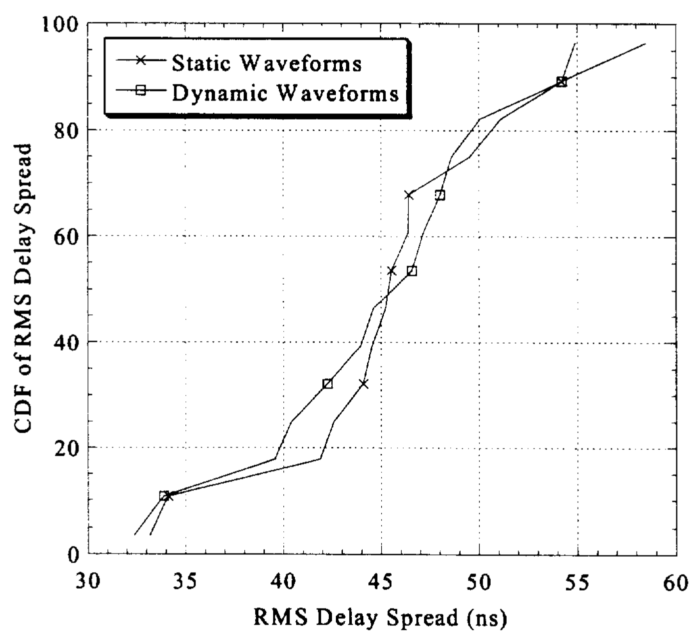

Figure 6-57: CDF of RMS delay spread, calculated over 300 ns window.

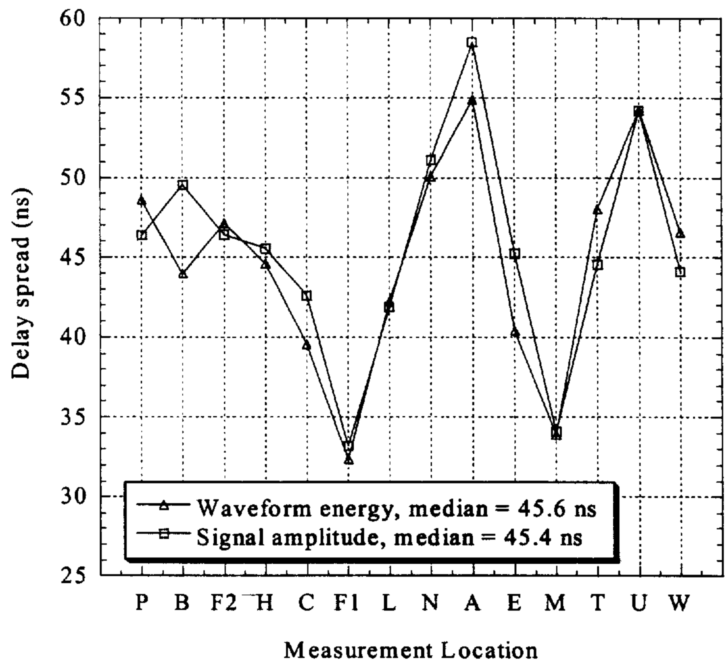

Figure 6-58: Delay spread as a function of measurement location. Results from the assumption that the signal energy is proportional to the recovered amplitude and from calculating the energy from the recovered waveform are shown.

Location	SNR (dB)	$\overline{T_a}$ (ns)	$\overline{T_r}$ (ns)	σ_T (ns)	$\overline{\phi}$ $(^o)$	σ_ϕ $(^o)$
P	31.93	72.96	52.11	46.38	17.95	66.41
B	11.56	112.89	53.86	49.53	4.01	60.92
F2	38.58	62.054	40.72	46.42	-7.80	54.00
H	18.88	91.59	54.97	45.52	1.30	48.45
C	13.76	110.32	50.26	42.58	32.49	68.39
F1	39.56	48.66	17.12	33.16	8.21	43.04
L	35.92	57.97	31.89	41.89	-5.43	33.68
N	25.98	67.16	46.90	51.12	7.78	65.24
A	-3.14	143.11	86.71	58.46	-42.94	79.52
E	-1.97	112.47	64.72	45.23	12.39	56.31
M	24.16	82.32	36.13	34.11	-12.22	50.14
T	21.08	93.05	55.50	44.53	16.69	66.24
U	15.69	104.69	66.85	54.20	22.52	87.87
W	23.09	84.03	51.85	44.09	0.52	56.35
Median	22.08	87.81	51.98	45.38	5.90	58.63

Table 6.3: Summary of propagation statistics when calculating energy from recovered signal amplitude

Location	SNR (dB)	$\overline{T}_a$ (ns)	$\overline{T}_r$ (ns)	σ_T (ns)	$\overline{\phi}$ $(^o)$	σ_ϕ $(^o)$
P	42.14	76.07	55.22	48.61	18.64	65.88
B	20.69	100.79	41.76	43.95	7.39	55.33
F2	48.35	61.22	39.88	47.16	-6.11	51.06
H	27.12	93.36	56.74	44.61	2.09	44.14
C	24.11	98.57	38.51	39.56	27.02	60.61
F1	48.86	48.56	17.01	32.34	7.67	40.80
L	46.13	57.00	30.93	42.25	-4.58	30.06
N	35.99	64.38	44.11	50.06	8.35	60.84
A	-0.31	137.96	81.56	54.88	-51.38	75.06
E	2.02	106.79	59.03	40.42	14.06	50.27
M	33.05	81.03	34.84	33.90	-11.53	50.39
T	29.98	97.46	59.91	48.01	12.51	64.33
U	24.47	109.43	71.59	54.22	23.81	89.98
W	33.87	85.65	53.47	46.57	1.31	51.10
Median	31.56	89.51	48.79	45.59	7.53	53.21

Table 6.4: Summary of propagation statistics when calculating energy from recovered waveforms

6.3.3 Joint Spatio-Temporal Channel Models

The moments of the angular and temporal distribution of the received signal energy provide a description of the channel statistics which assumes that no correlation exists between the two measures. In [48], and [49] it is argued that this is a sufficient description of the channel; that, based upon a visual inspection of the received signal locations over time and angle, no apparent dependency exists. The goal of this section is to determine the extent to which this assumption holds for the UWB propagation experiment under consideration. It is important to note that the claim of time-invariant statistics given in [48] and [49] did not take into account the energy in the signal arrivals, but only the fact that an arrival had taken place. In the calculation of $\overline{\phi}$, $\overline{T}$, σ_ϕ and σ_T, on the other hand, the arrival statistics are weighted by the received signal energy. Contrary to the scatter diagram used to assess these statistics in [48] and [49], a weak arrival does not carry the same weight in $\overline{\phi}$, $\overline{T}$, σ_ϕ and σ_T as does a higher energy arrival.

As a first measure of the time-variation of the UWB propagation channel, consider Figure 6-59 which shows the rms angular spread for the fourteen measurement locations as a function of time, using 10 ns wide bins to collect the received signal energy. The plot in (a) shows the results if no window is applied to the angular deviation from the mean, and in (b) a raised-cosine window is applied to the difference between the azimuth arrival angle of the received signal and the mean arrival angle. The purpose of this window is to limit the effect that a signal incident from a large angular deviation can have on the statistics. Overlaid onto each of these plots is the mean rms angular spread and $\pm 1\sigma$ bounds. From the plots it can be seen that the rms angular spread does vary as a function of time, taking on a broader range of values as time progresses. The cumulative distribution functions of the angular spread are shown in Figure 6-60, with and without a raised cosine filter on the angular deviation from the mean. This plot shows the ranges of values taken on by the angular spread over the 300 ns window. It is clear from these plots that the angular spread is not static, but does take on different values as time progresses.

In the plots it is noted that the angular spread increases as a function of time, to a point, then decreases near the end of the 300 ns window. This decrease is an artifact that is due to the data from some measurement locations containing no signal arrivals in these late time bins. These measurement locations then contribute nothing to the mean calculation, which reduces the value.

6.3.4 Spatio-Temporal Distributions

In order to describe the spatio-temporal properties of the channel, the cumulative distribution function (CDF) for the incident UWB signals is calculated from the recovered signal information. First consider the distribution functions which results from a uniform weighting of all arrivals, assuming that all signals are incident with equal energy. This will allow for a further examination of the time variance of the UWB channel statistics against the claim of time-invariance made in [48] and [49]. This is shown for the measurement at location P in Figure 6-61 and location B in Figure 6-62. A noticeable difference between the plots is the arrival time of the first component, caused by the difference in the LOS path length between the two sets of measurements. Considering the time variation in the response of these channels, the marginal CDF for the two locations is shown in Figure 6-63 and Figure 6-64 along with a uniform CDF. The direction of increasing time is shown, and the degree to which the distributions change as a function of time is noted. The recovered signals from measurement location P are seen to be distributed more uniformly than those from location B. This was also noted in Figure 6-2 - Figure 6-10.

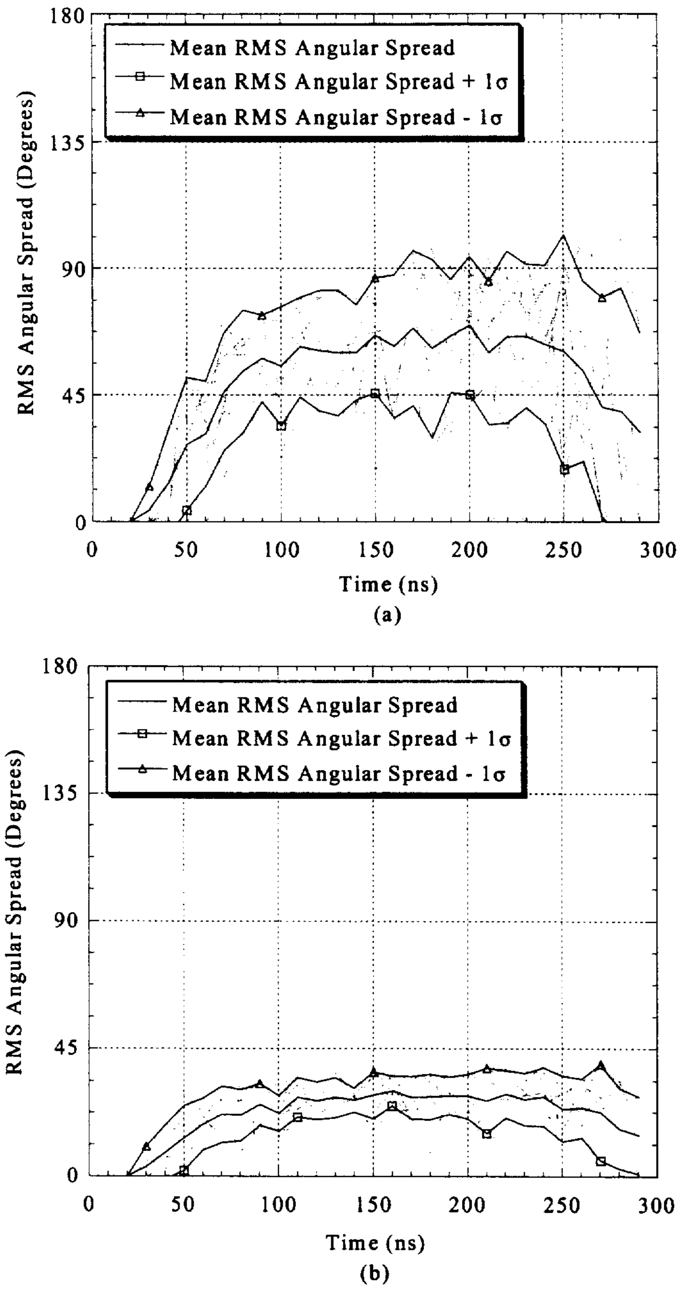

Figure 6-59: Power weighted rms angular spread (a) without and (b) with a raised cosine window for the 14 measurement locations. Mean angular spread and mean $\pm$ 1σ is overlayed.

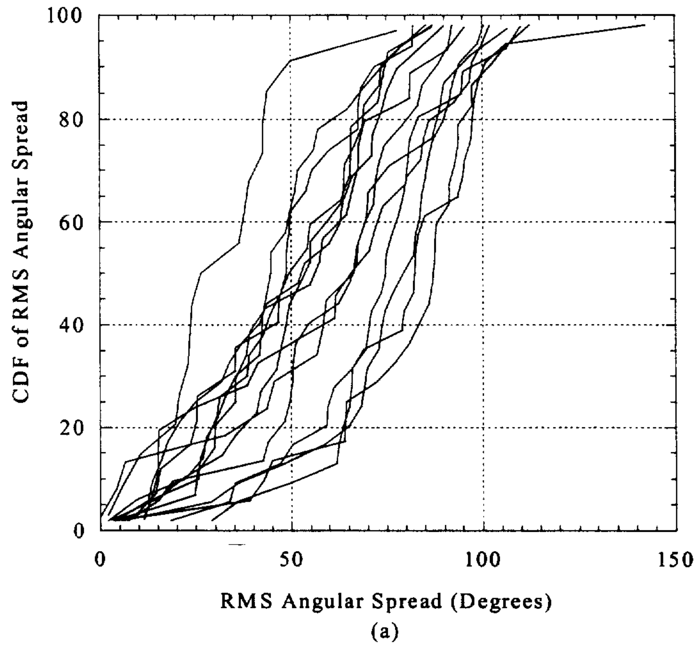

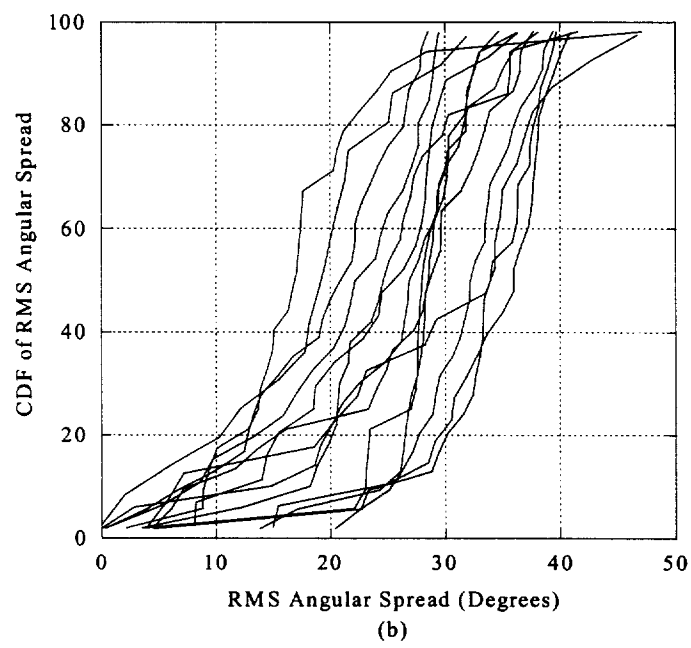

Figure 6-60: CDF of RMS angle spread calculated in 10 ns windows, for the 14 measurement locations. A raised cosine filter is applied to the results in (b).

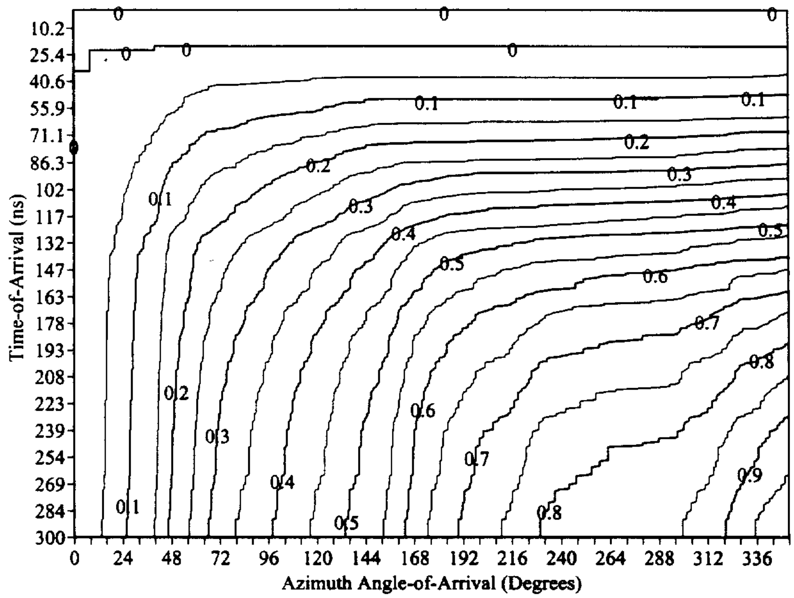

Figure 6-61: Distribution of incident signals at location P, with uniform weighting on each signal arrival.

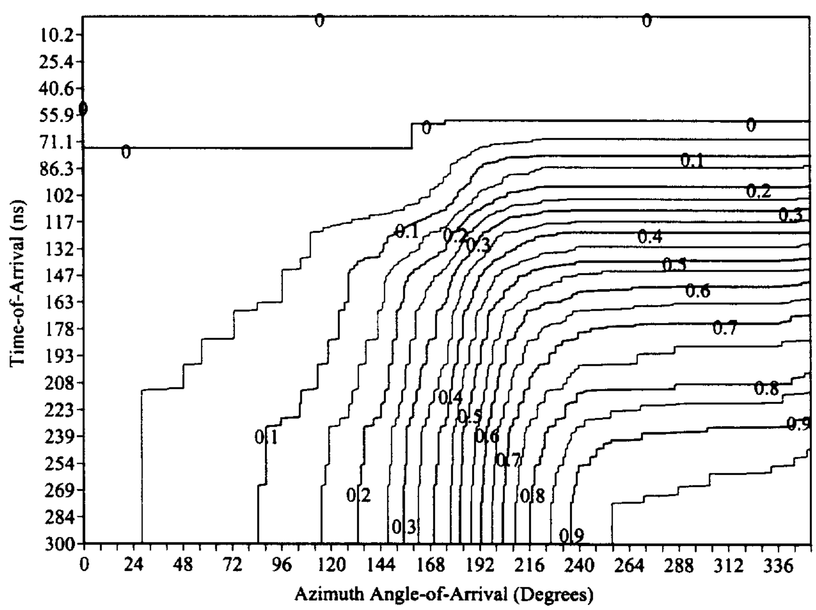

Figure 6-62: Distribution of incident signals at location B, with uniform weighting on each signal arrival.

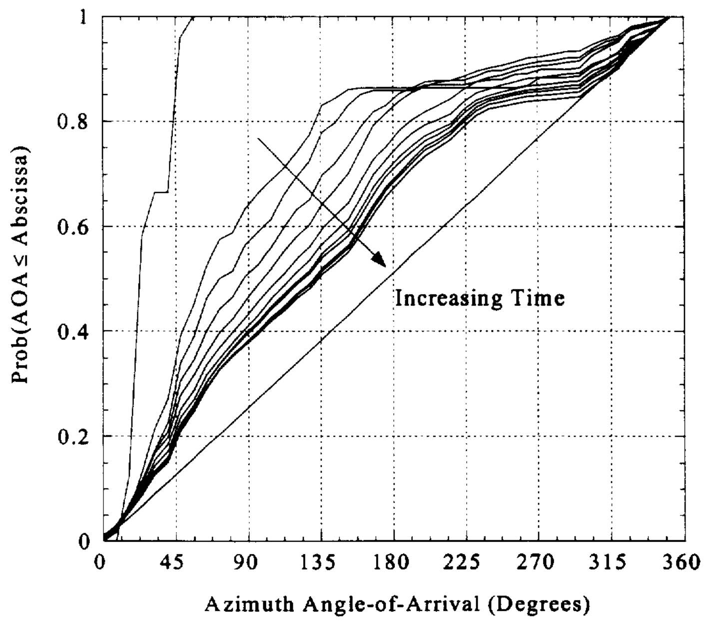

Figure 6-63: Marginal distributions as a function of time for the measurements at location P. A uniform distribution is also shown.

If all measurement locations are considered and the angle-of-arrival of each component is reported relative the angle-of-arrival of the LOS path for the particular measurement location, the resulting CDF of the signal arrivals is shown in Figure 6-65. The marginal distributions as a function of time are shown in Figure 6-66. It is clear from these plots that the statistics associated with a uniform weighting of the signals in the distribution do vary to some extent as a function of time for the UWB propagation channel under consideration.

In the interests of predicting communication system performance, it is not only the existence of a signal at a particular location in time and space that matters, but the energy carried by the signal as well, for a given noise level. For example, the bit error rate of a communication system is generally characterized by the bit energy to noise spectral density ratio, and is independent of other parameters related to the propagation channel. This motivates the study of the spatio-temporal distribution of the received signal energy. Define the distribution functions in this case by assigning a weight to each incident signal proportional to the recovered energy. For an angular increment of $\Delta\theta$ and a sampling frequency of $\frac{1}{\Delta t}$ seconds, this weighted cumulative

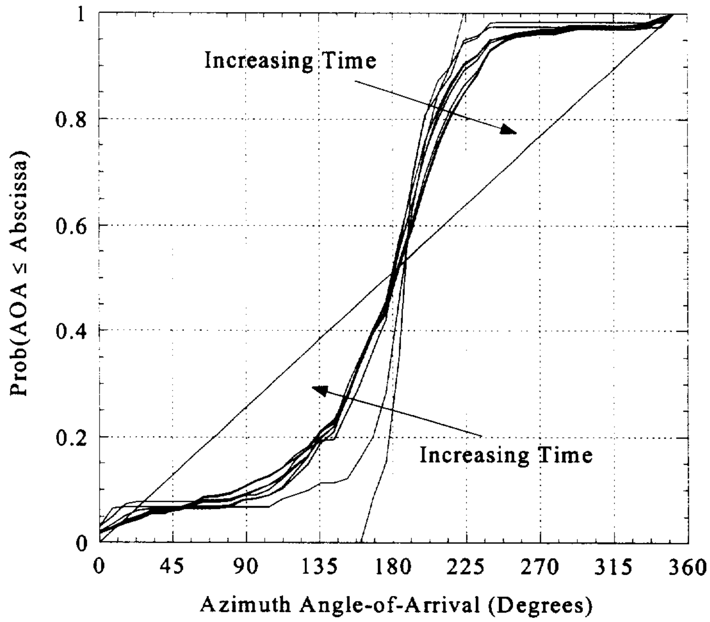

Figure 6-64: Marginal distributions as a function of time for the measurements at location B. A uniform distribution is also shown.

distribution function (CDF) is then calculated according to

$$
\begin{aligned}
F_{\theta,\tau}(k,n) &= \Pr\{\theta \leq k\Delta\theta, t \leq n\Delta t\} \\
&= \frac{1}{E}\sum_{j=0}^{k}\sum_{m=0}^{n}\beta_{m,j}^{2}
\end{aligned}
\tag{6.16}
$$

where $k = 0, ..., K-1$, $n = 0, ..., N-1$, and $\beta_{m,j}^2$ has the same meaning as above, it is the energy in the received signal, either corresponding to the square of the amplitude of the component found at time m and angle j under an assumption of static incident waveforms, or as computed from the recovered waveform. The quantity E is the total recovered energy in all signal components, resulting from allowing the summations to run over the entire data collection window in time and in angle. Distributions calculated according to 6.16 will be referred to as (energy) weighted distributions or weighted cumulative distribution functions (CDFs), to distinguish them from distributions which account only for signal arrivals.

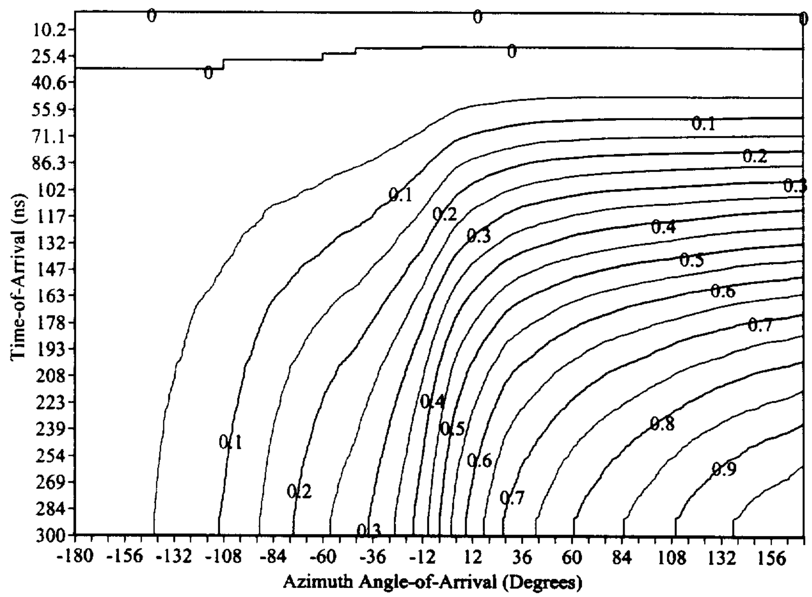

Figure 6-65: Distribution of incident signals from all locations, with uniform weighting on each signal arrival. All angles are relative to LOS angle-of-incidence for the measurement location.

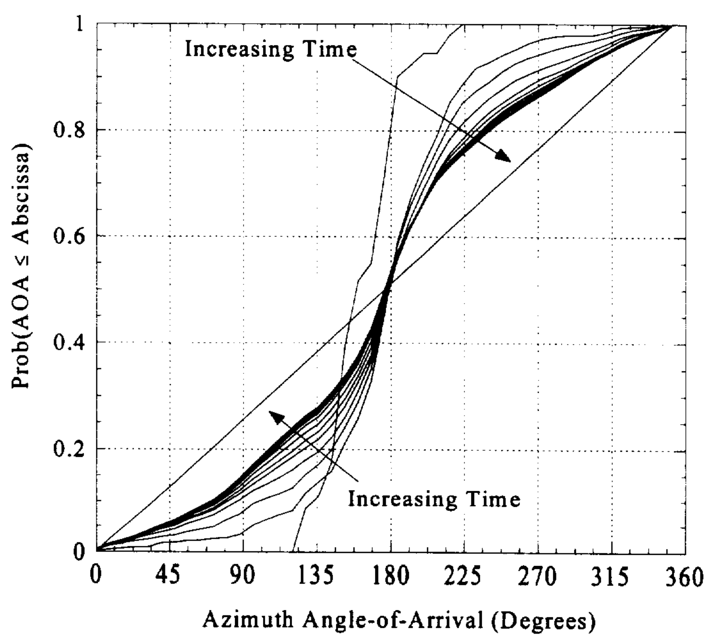

Figure 6-66: Marginal distributions as a function of time for the measurements at all locations. Each recovered signal contributes equally to the distribution functions. A uniform distribution is also shown.

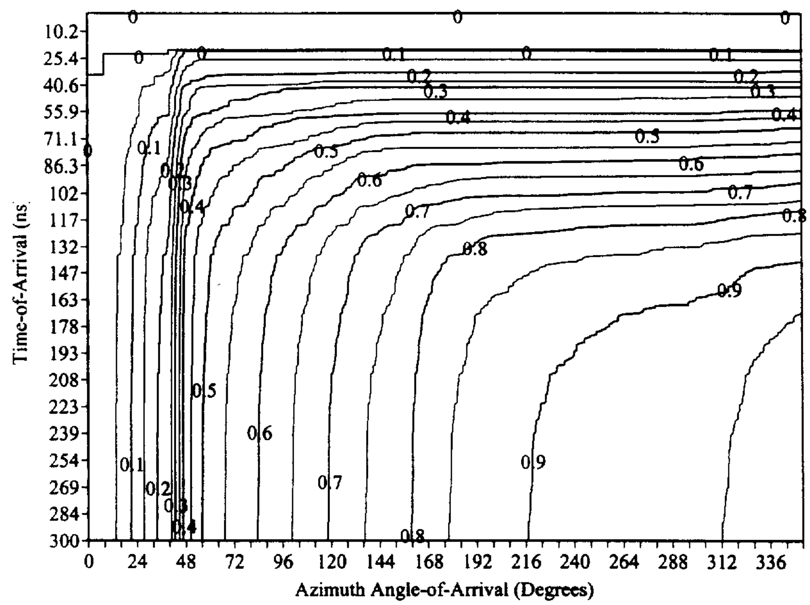

Figure 6-67: Weighted distribution of the received signal energy at location P when estimated from the recovered waveforms.

Examples of the weighted CDF for measurement locations P and B are shown in Figure 6-67 and Figure 6-68, respectively. In both of these figures, it is noted that the recovered signal for azimuth angles close to the LOS path contributes significantly to the total received signal energy, and the distribution is therefore less uniform than those in Figure 6-61 and Figure 6-62, where all signals were weighted equally.

As another case of interest, consider Figure 6-69, which shows the weighted CDF of energy arrival at location A, the measurement location with the lowest SNR. As demonstrated above, the algorithms had a great deal of difficulty estimating the waveform of the LOS path in this case. Even in this low SNR case, although the received signal energy is distributed more uniformly than the energy recovered either at location A or P, it is still biased around the LOS arrival angle.

As above, it is of interest to determine a measure of average performance or an average distribution which takes into account all measurement locations. There are two ways to consider this average. The first is to maintain the absolute relation in the total recovered energy between the measurement locations. The contribution from each location is then weighted in the

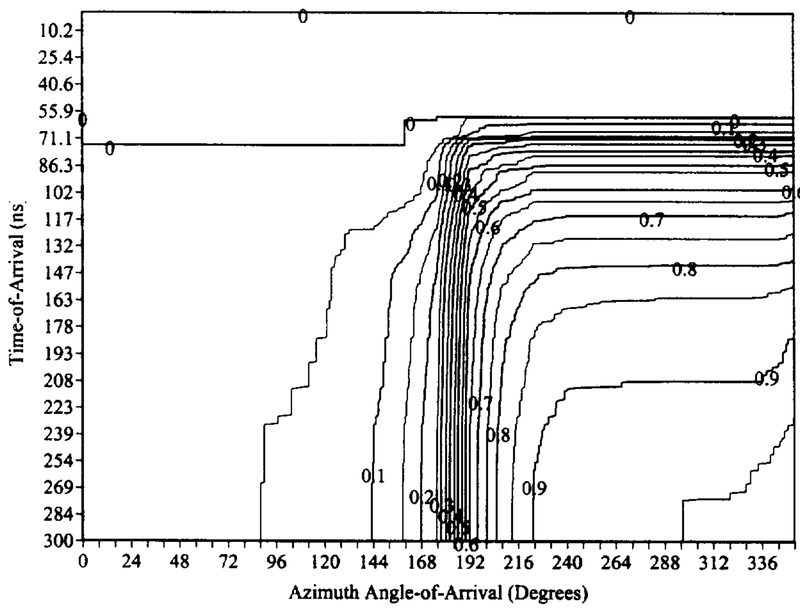

Figure 6-68: Weighted distribution of the received signal energy at location B when estimated from the recovered waveforms.

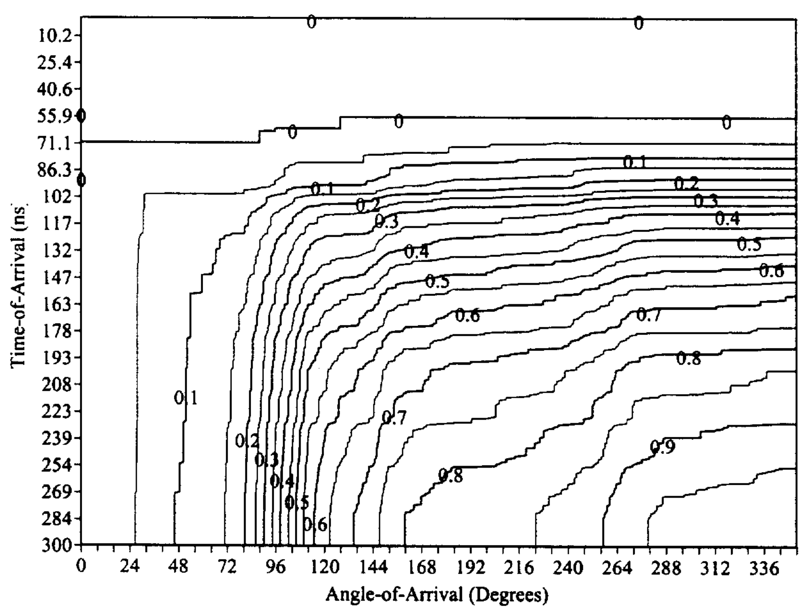

Figure 6-69: Weighted distribution of the received signal energy at location A when estimated from the recovered waveforms.

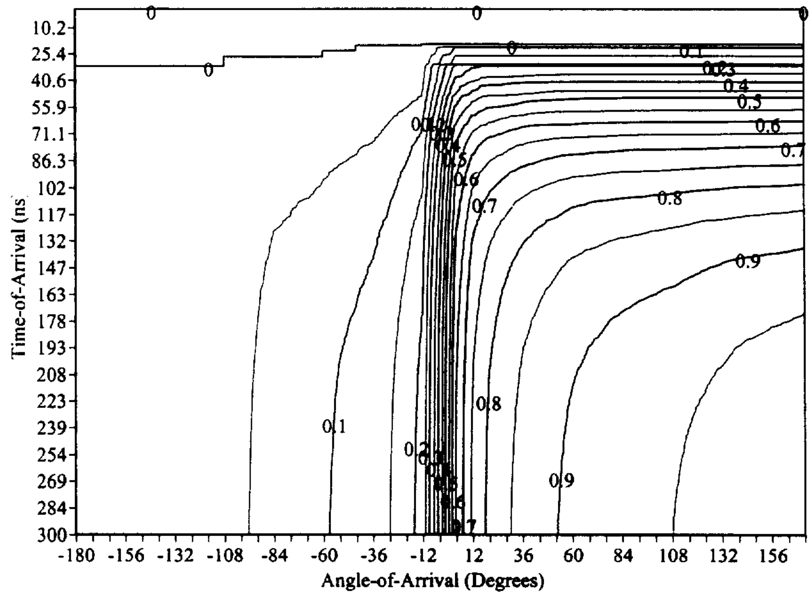

Figure 6-70: Weighted distribution of received signal energy over time and angle for all measurement locations. Energy is calculated from recovered waveforms.

distribution function by the recovered energy at the location divided by the energy recovered from all locations. The weighted CDF which results from maintaining this absolute relation between the recovered signal energies is shown in Figure 6-70, where all angles are reported relative to the LOS path arrival angle for the particular measurement location. The second approach is to generate a distribution function under the assumption that the channel or location within the building is selected randomly from all possible locations. This might be an appropriate assumption in a mobile scenario, where the receiver is equally likely to be at any location in the building. In this case all channels contribute equally to the overall distribution, each getting a weight of 1/14 here, for the 14 different measurement locations. Within the distribution function for each channel, individual components are weighted according the signal energy. The distribution function associated with this scenario is shown in Figure 6-72, where again all angles are reported relative to the LOS path for the particular measurement location. Marginal distribution functions associated with these spatio-temporal distributions are shown in Figure 6-71 and Figure 6-73.

The results above are useful in terms of understanding the effect of the channel on

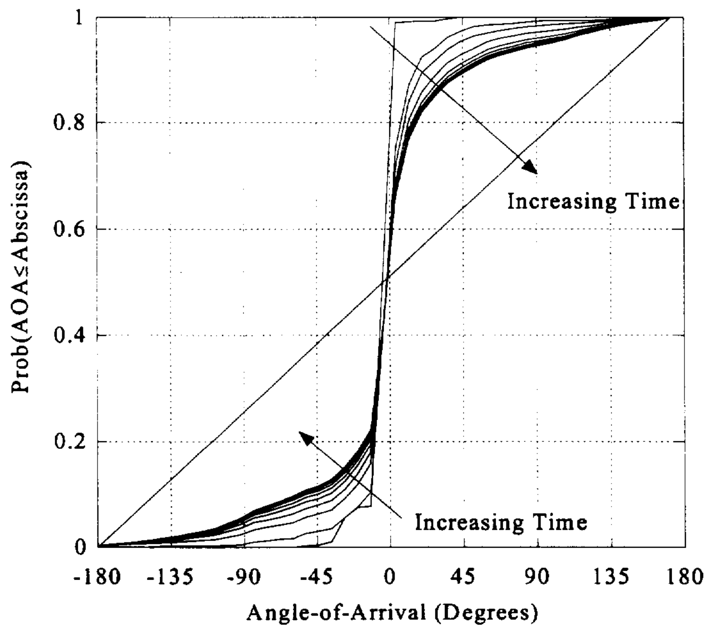

Figure 6-71: Marginal distribution functions vs. time. Each measurement location contributes an amount proportional to the received energy at that location divided by the total received energy.

propagating UWB signals. However, these results can exhibit a bias due to a large number of signals without enough energy to provide a reliable communication link, but with enough energy collectively to generate a noticeable effect on the distributions. In order to further the practical significance of the results, additional constraints were therefore placed on the contributing signals. In particular, two constraints were considered. The first involves the realization that diversity reception is of interest in the indoor multipath channel. In a typical rake receiver, some finite number of correlators are available for the processing the received signals. Therefore the distribution of the received signal energy contained in some number of the strongest paths is of interest. For the purposes of this work, ten paths were selected. The weighted distribution of the signal energy in the ten strongest paths from all measurement locations is shown in Figure 6-74 and Figure 6-75 for the absolute and equiprobable channel cases, respectively.

Given that a rake receiver might not always select the strongest available paths or that these paths may be transient, particularly in an indoor or shadowed environment, the distribution functions were also characterized by only allowing signals within some number of

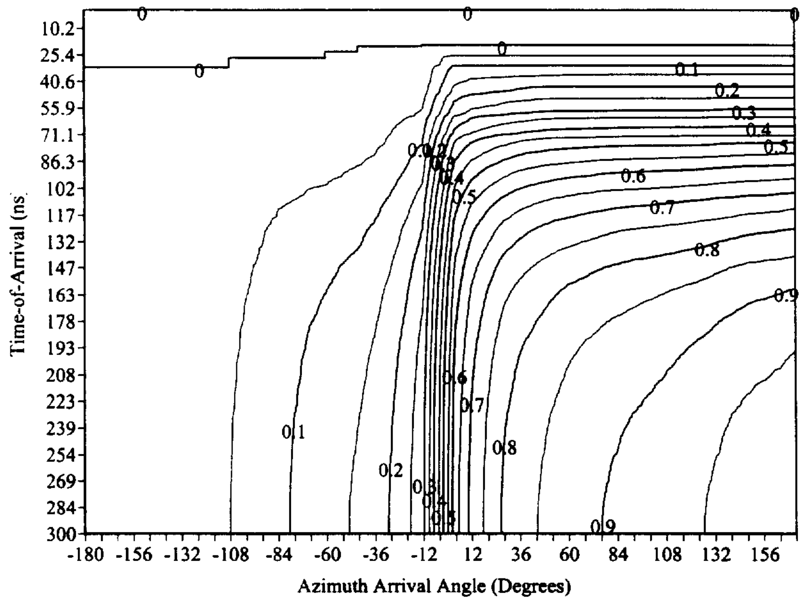

Figure 6-72: Weighted distribution of received signal energy over time and angle for all measurement locations, where each location contributes equally. Energy is calculated from recoverd waveforms.

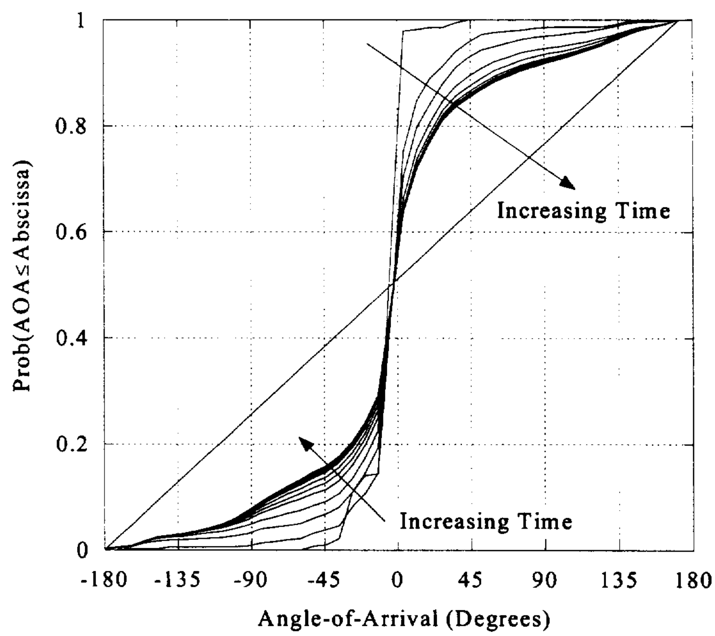

Figure 6-73: Marginal distribution functions vs. time for the case where each measuement location contributes an equal amount to the distributions.

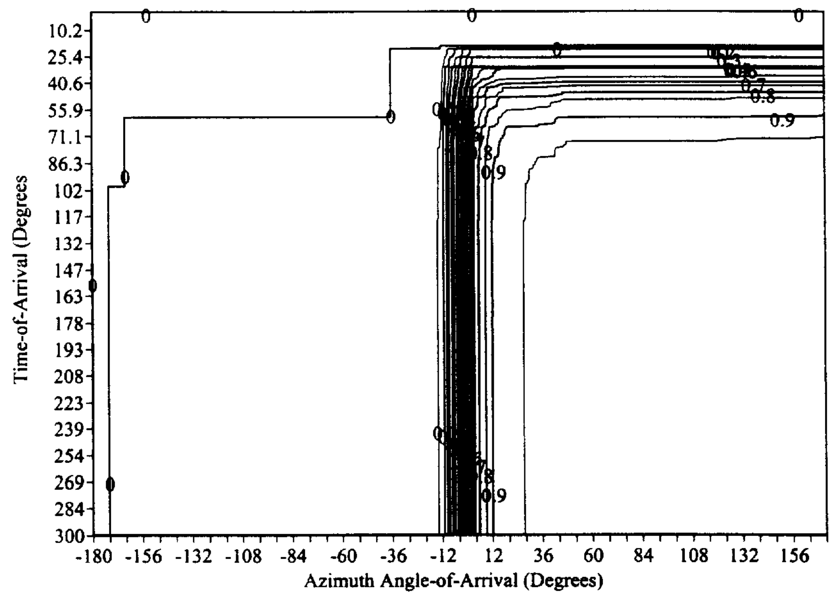

Figure 6-74: Weighted distribution of received signal energy over time and angle for all measurement locations, where only the largest ten signals at each location are considered.

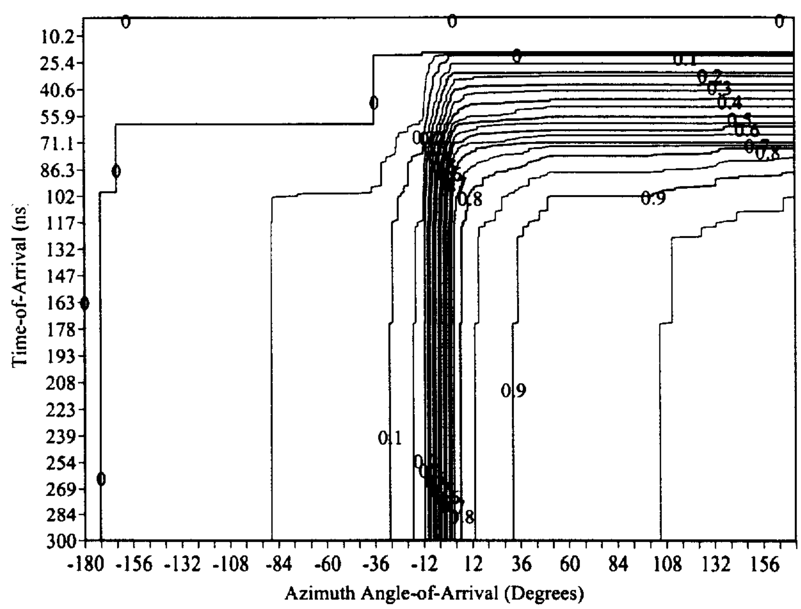

Figure 6-75: Weighted distribution of received signal energy over time and angle for all measurement locations, where only the largest ten signals at each location are considered. The contribution from each measurement location is weighted equally.

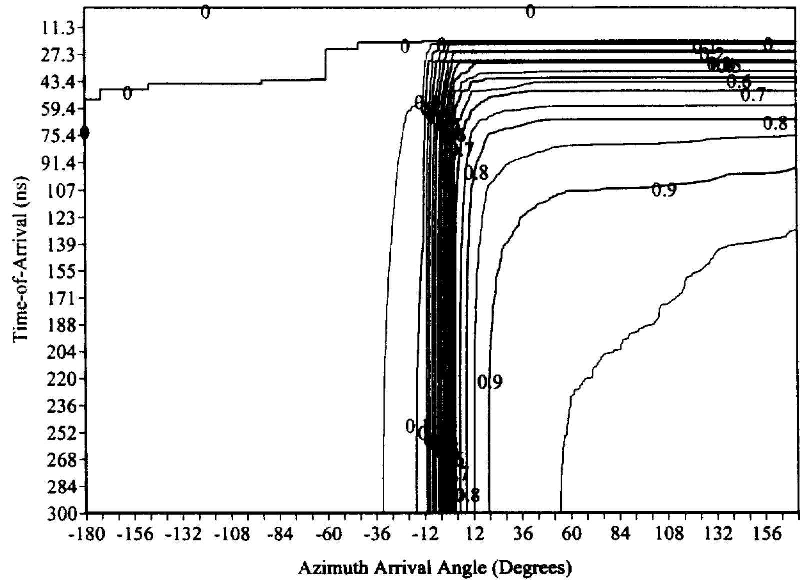

Figure 6-76: Weighted distribution of received signal energy over time and angle for all measurement locations, where only signals with received energy within 12dB of the largest signal at each measurement location are considered. The contribution from each measurement location is weighted equally.

decibels of the strongest arrival in each measurement location to contribute. For the results presented here, all signals within 12 dB of the strongest arrival in each measurement location were allowed to contribute to the weighted distribution functions. These results are shown in Figure 6-76 and Figure 6-77.

From a visual inspection, the threshold based on the signal energy rather than on the absolute number of contributing paths seems to have the effect of increasing the variance of the distribution slightly. This is due to the fact that the energy threshold permits more signals to contribute to the distribution. In general, however, both of these thresholds seem to lead to the same conclusion that the bulk of the recovered signal energy is contained in a relatively small range of arrival angles around the LOS path arrival angle.

Weighted distribution functions were also generated under the assumption of static incident waveforms, where the energy is calculated from the recovered signal amplitude information only. These are shown below in Figure 6-78 - Figure 6-83.

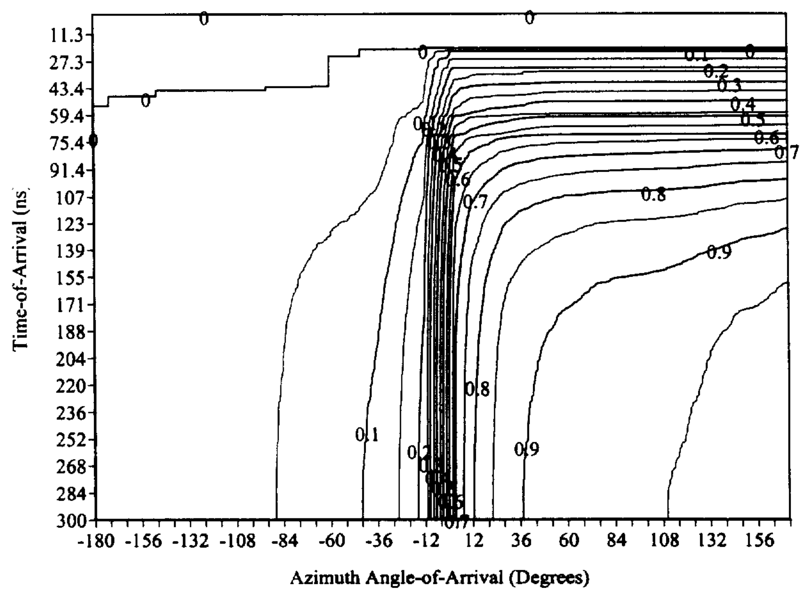

Figure 6-77: Weighted distribution of received signal energy over time and angle for all measurement locations, where only signals with received energy within 12dB of the largest signal at each measurement location are considered. The contribution from each measurement location is weighted equally.

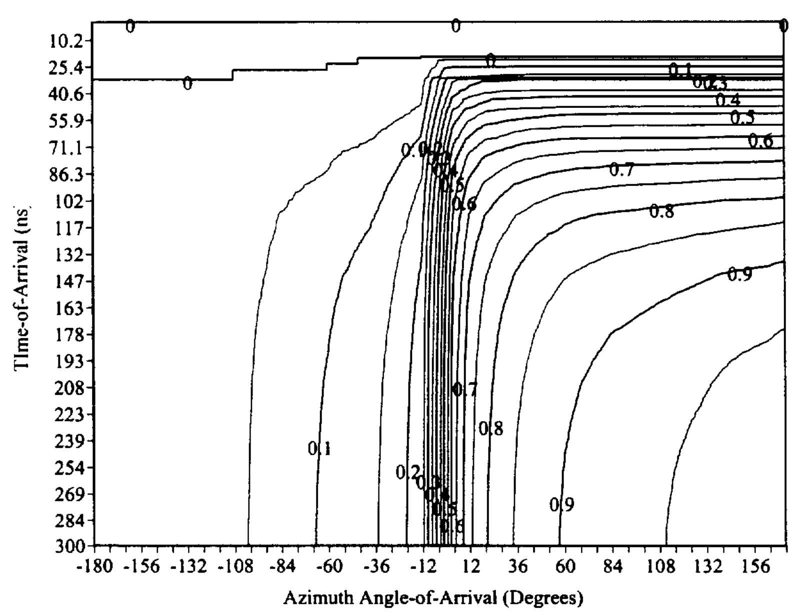

Figure 6-78: Weighted distribution of received signal energy over time and angle for all measurement locations. Energy is calculated from recovered signal amplitude.

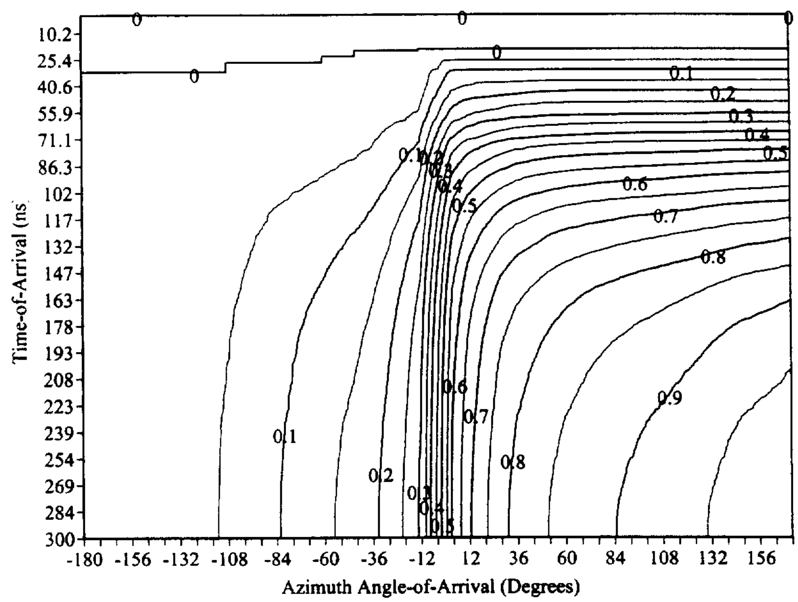

Figure 6-79: Weighted distribution of received signal energy over time and angle for all measurement locations. Each location contributes equally to the distribution. Energy is calculated from recovered signal amplitude.

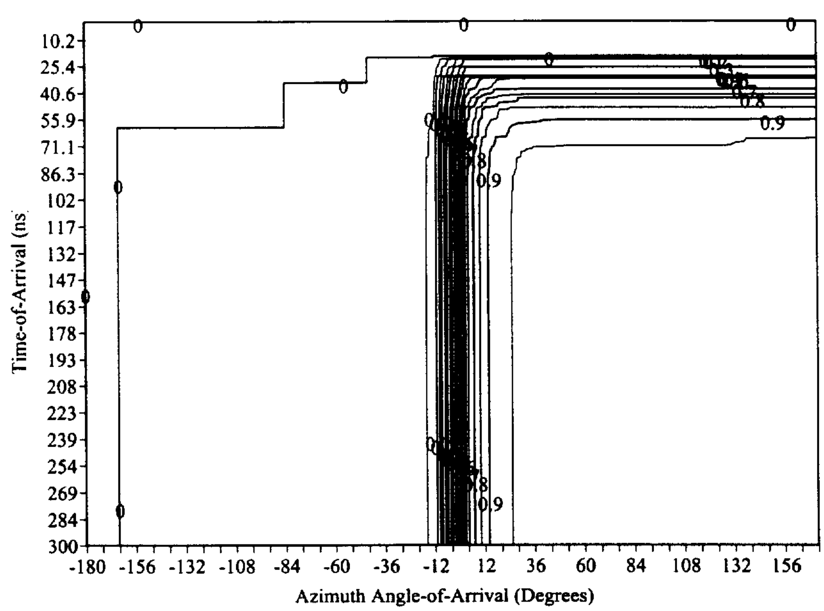

Figure 6-80: Weighted distribution of received signal energy over time and angle of the ten largest signals at each measurement location. Energy is calculated from recovered signal amplitude.

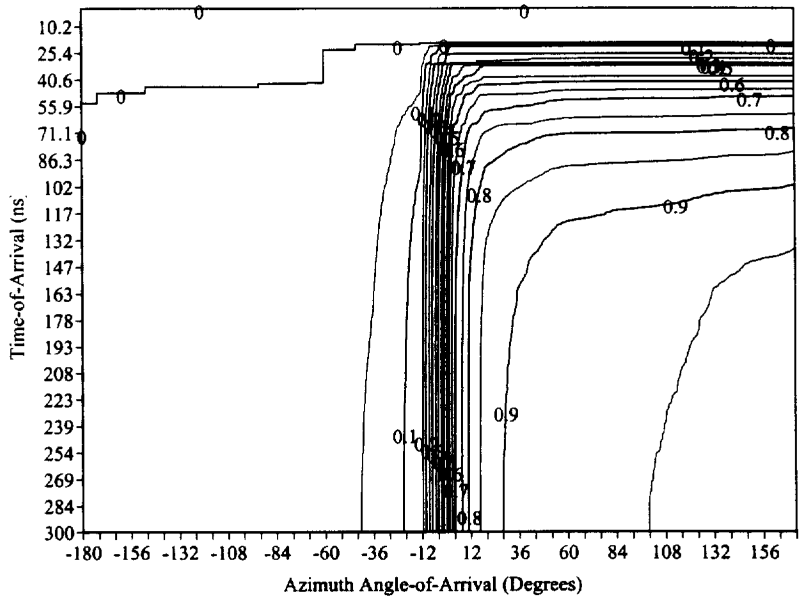

Figure 6-81: Weighted distribution of received signal energy over time and angle for all signals with energy within 12dB of the largest signal at each location. Energy is calculated from recovered signal amplitude.

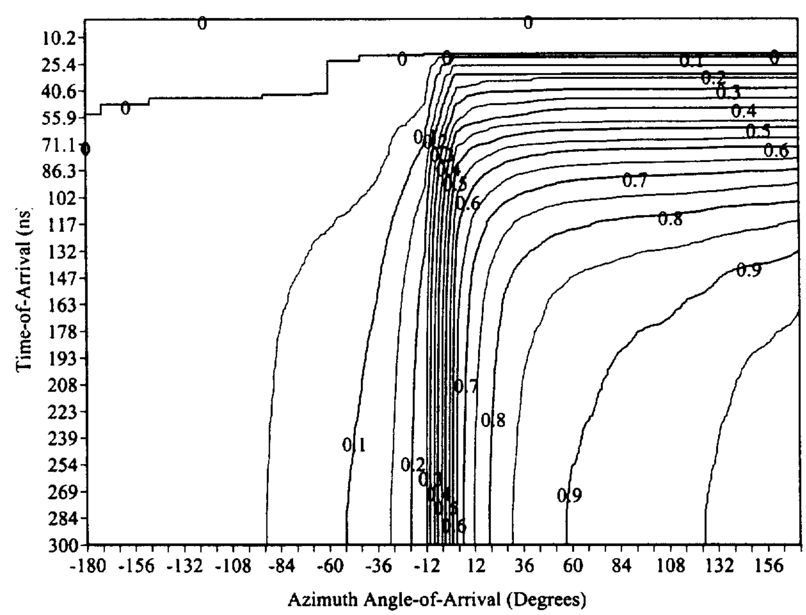

Figure 6-82: Weighted distribution of received signal energy over time and angle for the ten largest signals at each measurement location. Each location contributes equally to the distribution. Energy is calculated from recovered signal amplitude.

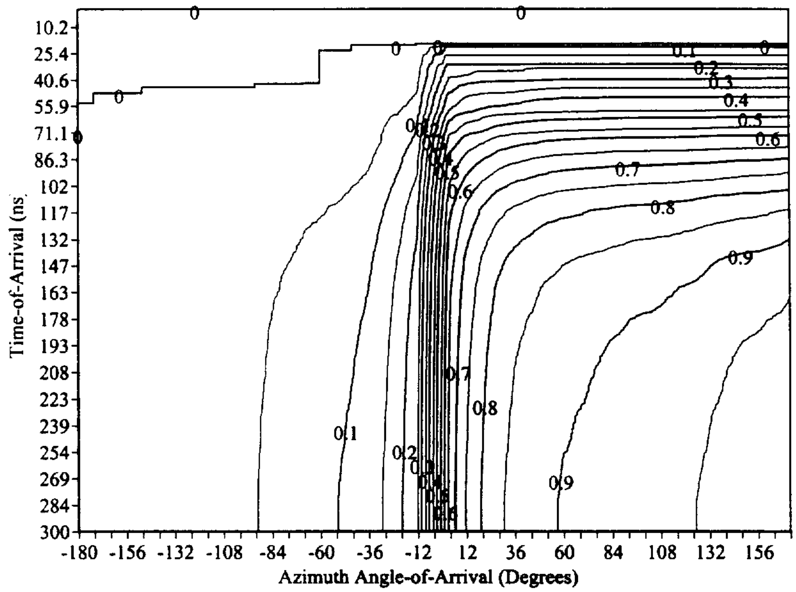

Figure 6-83: Weighted distribution of received signal energy over time and angle for all signals within 12dB of the largest signal at each measurement location. Each location contributes equally to the distribution. Energy is calculated from recovered signal amplitude.

6.4 Summary

In this chapter, the processing techniques developed in Chapter 4 and Chapter 5 were applied to the measured propagation data described in Chapter 1. The resulting signal information was used to develop models of the indoor UWB propagation channel. Several different models were developed to analyze different aspects of the UWB propagation problem. When comparable parameters existed, comparisons were drawn with more narrowband channel models from the literature.

The characterization provided in this chapter for the UWB propagation channel reflects measurement made at a number of locations in a single building. As has been reported in previous propagation experiments, the architecture of the building and the geometry of the particular situation can often have a strong impact on the received signals. As these results are based upon measurement taken in a single building, it is possible that additional experiments will need to be conducted in different buildings in order to increase confidence in the parameters of a propagation model. It is possible, then, that although this work presents a propagation model for UWB signals in an indoor environment, the strongest contribution of this research will be in the development of a technique to facilitate the high-resolution analysis and processing of received UWB signals.

Chapter 7

Further Results on the Characterization of the UWB Propagation Channel.

In the previous chapter, channel models were derived to describe the spatio-temporal distribution of the received UWB signal energy in an indoor environment. In this chapter, further studies are conducted on the recovered signal information from the processing algorithms. These include a ray-tracing study based on the angle-of-arrival of the received signal and the orientation of the transmitter and the receiver, under the assumption of a single-bounce elliptical model. This information may prove useful in the development of diversity reception schemes.

In addition to angle and time-of-arrival information, the Arrival Combiner also generates estimates of the received signals. These are examined here as well, in order to understand typical variations in the received pulse shape encountered in the indoor channel.

This chapter ends with an attempt to synthesize an UWB propagation channel based upon the cluster models from the previous chapter. The ability to accurately synthesize UWB propagation channels is significant in that it gives a realistic environment in which UWB radio algorithms can be tested and verified in software.

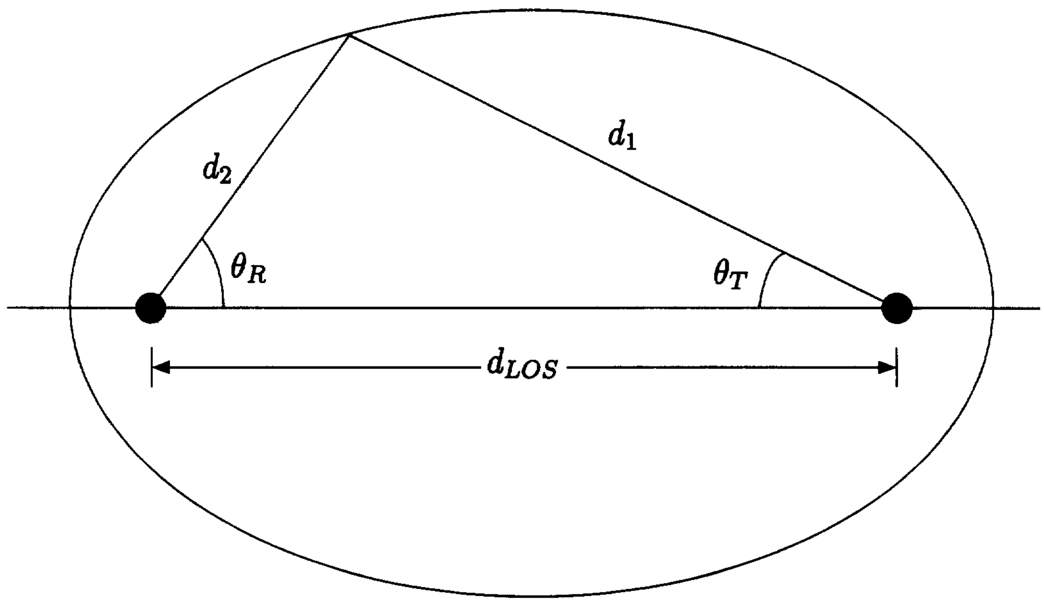

Figure 7-1: Ellipse which describes signal reflection

7.1 Ray tracing (Implications for Diversity)

Considering the applications for UWB radio discussed in Chapter 1, it is of interest to examine diversity algorithms for these systems. In particular, for the indoor environment, a useful performance measure is the ability of UWB communication systems to overcome transient blockages in the received signal paths, through the coherent addition of multipath signal components in a rake-type receiver. Given this measure, the resources required to maintain a communication link with a certain probability can be calculated.

Consider the transmitter and receiver pair shown in Figure 7-1, where the ellipse describes the locus of reflectors for all paths of identical propagation length corresponding to a single reflection. Let θ_T represent the angle at which a signal component emanates from the transmitter, and let θ_R represent the received angle. Given θ_R, the signal propagation distance and the LOS propagation distance, the angle θ_T at which the component is transmitted can be uniquely determined, based on the assumption of a single reflection.

Denote the LOS propagation distance by d_{LOS}, and the total propagation distance of the signal by $d = d_1 + d_2$. The eccentricity of the ellipse is then given by $e = d_{LOS}/d$. Defining

$$l = 0.5\left(d - \frac{d_{LOS}^2}{d}\right), \tag{7.1}$$

the distance d_2 can be calculated according to

$$d_2 = \frac{l}{1 - e\cos(\theta_R)}. \tag{7.2}$$

The angle θ_T is then given by

$$\theta_T = \cos^{-1}\left(\frac{d_{LOS} - d_2\cos\theta_R}{d - d_2}\right) \tag{7.3}$$

where this angle must be reflected about the major axis of the ellipse if θ_R is negative.

In practice, the utility of this approach is limited by the lack of an analytic technique for discriminating signal components which arrive at the receiver after a single reflection from those corresponding to multiple reflections. At present, this is accomplished either by correlating the calculated locations of the reflectors against the floor plan or by incorporating filters on the overall path length $d = d_1 + d_2$ or on the height at which the reflection occurs. The latter condition requires the received elevation angle to be incorporated into the calculations. From the received elevation angle,ϕ_2, the elevation angle at which the signal emanates from the transmitter can be calculated as,

$$\phi_1 = \cos^{-1}\left(\frac{d_2}{d_1}\cos\phi_2\right). \tag{7.4}$$

The vertical distance from the array to the point at which the reflection occurs, under the single-bounce elliptical model, is then $d_1\cos\phi_1$. Assuming that the signal does not penetrate the ceiling or the floor, this parameter can be used to place a filter on the calculated location of the reflections, based upon the physical realities of the building.

The location of the reflections in the building calculated this way are shown for two different cases below. In both figures, the transmitter is located at the origin of the coordinate system,

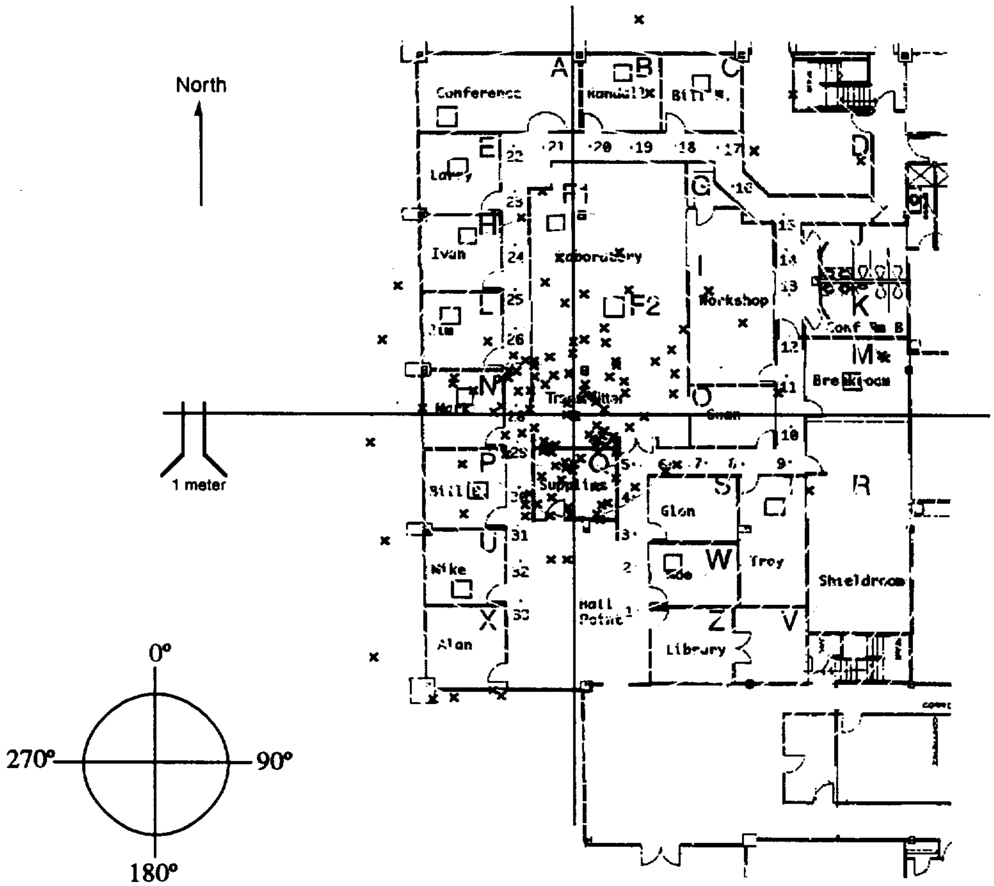

Figure 7-2: Calculated location of reflection for a single bounce elliptical model. The ten largest signals at each measurement location are considered.

and the calculated location of the reflections are indicated throughout the building. Figure 7-2 shows the calculated reflection locations if the ten largest signals at each measurement location are considered. Figure 7-3 shows the results of the same calculations if all signals within 12 dB of the largest signal at each measurement location are considered. As can be seen from these plots, is difficult to draw meaningful conclusions regarding these results. One interesting note is that the corners of the rooms, particularly those closest to the transmitter do seem to be a likely place for a reflection to occur.

Potential advantages of UWB communication systems which employ baseband signals in the indoor environment include the ability to penetrate obstructions and the fine multipath

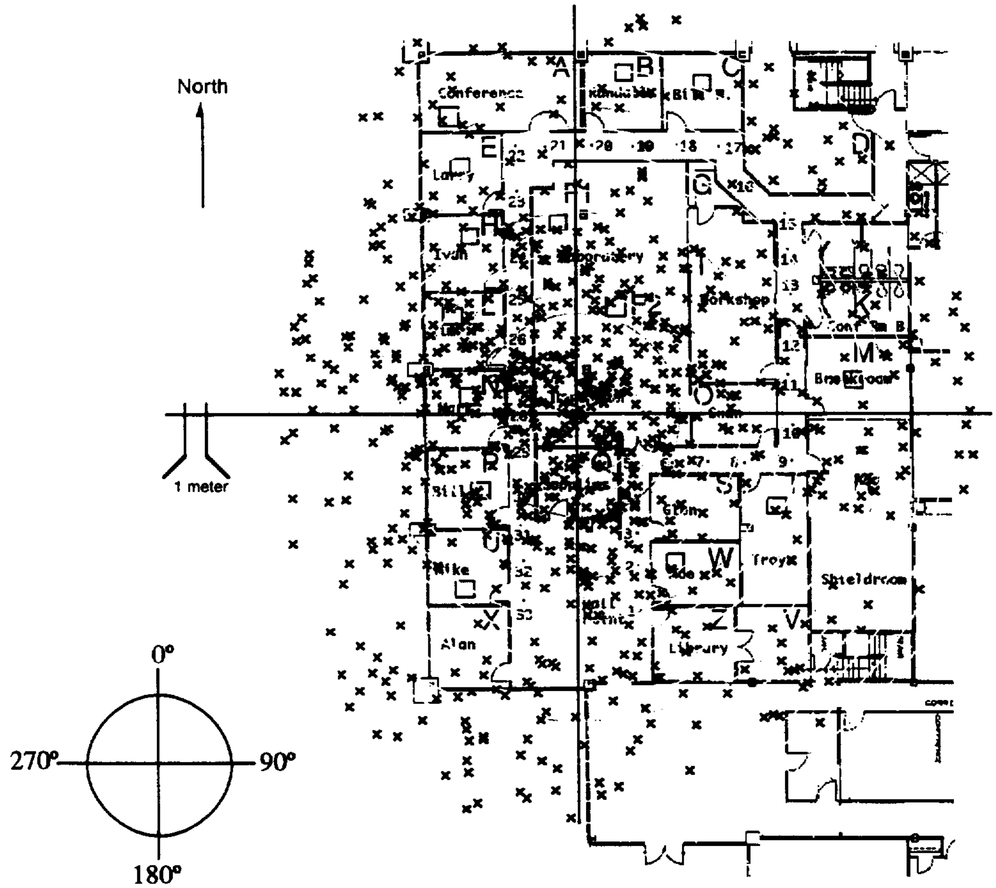

Figure 7-3: Calculated location of reflection for a single bounce elliptical model. All signals within 12dB of the largest signal at each measurement location are considered.

resolution afforded by the narrow pulse width. These properties are useful since they increases the probability that a signal path will exist between the transmitter and the receiver. In general, the greater the angular spread of distinct paths between the transmitter and the receiver, the greater the probability of overcoming a transient blockage in the signal path, or equivalently, the lower the probability that all paths are not available.

In Figure 7-4 and Figure 7-5, the incident signal azimuth angle-of-arrival and the calculated transmit angle are shown for the ten largest paths at each measurement location and for all detected signals within 12 dB of the largest arrival, respectively. The effect of the single bounce elliptical model on the results is noted immediately in the results. For example, a transmit

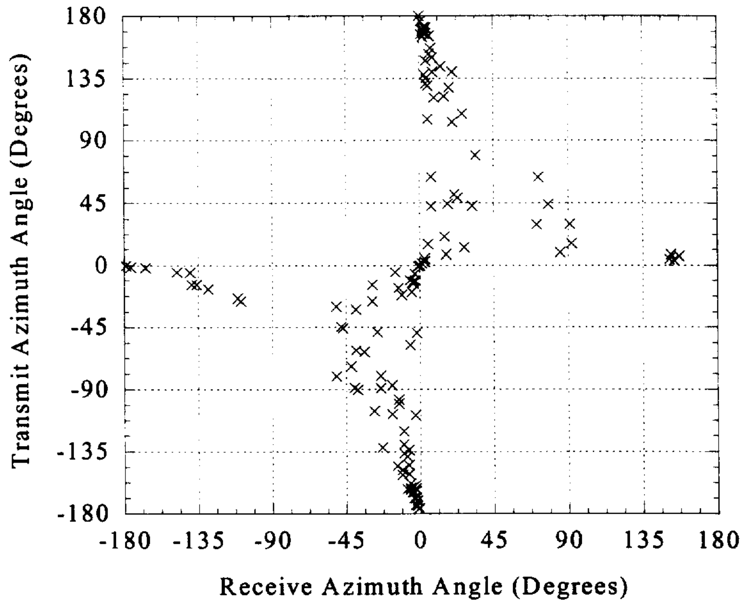

Figure 7-4: Recovered azimuth angle-of-arrival vs. calculated transmit angle for the single bounce elliptical model. The ten largest signals from each measurement location are considered.

and receive angle pair must both be either in the range from 0° to 180° or from 0° to -180°. The propensity of the reflections to occur close to the line-of-sight path, either at a transmit azimuth angle of 0° or 180°, and a corresponding receive azimuth angle of 0° or 180°, is also noted.

Considering the figures, for each azimuth angle at which a signal is received, the range of transmit angles which can give rise to this receive angle in the measured data is seen. The ability of an UWB communication system operating in this channel to overcome transient blockages or obstructions is a function of this angular spread.

7.2 Received Waveforms (Eye-Diagrams)

When designing receivers for a communication system, it is important to understand the effect of the channel upon the transmitted signals, or, equivalently, to understand what the received signal is expected to look like. The receiver will generally include a filter or a correlator matched to the anticipated form of the received signal. A result with practical significance is therefore

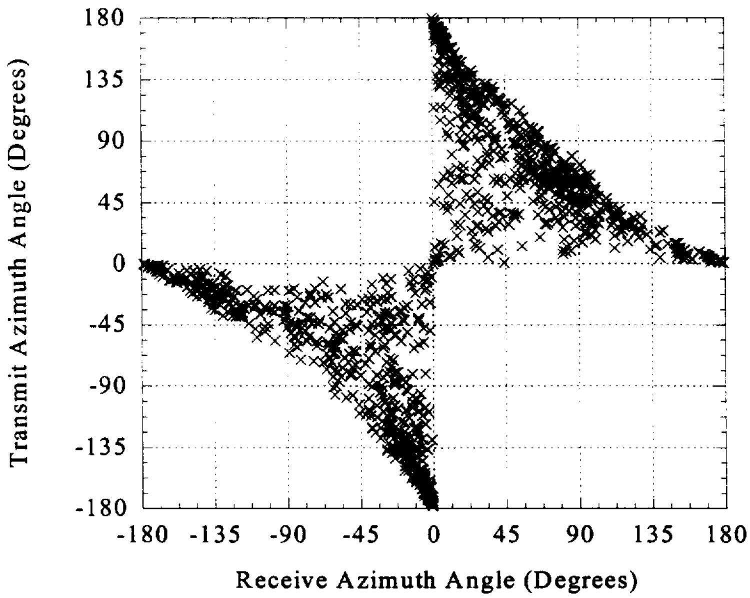

Figure 7-5: Recovered azimuth angle-of-arrival vs. calculated transmit angle for the single bounce elliptical model. All signals within 12dB of the largest signal at each measurement location are considered.

a characterization of the actual shape of the UWB signals received in the indoor environment. This information may find utility in the design of receivers for UWB communication systems.

Considering first the signal which arrives along the direct path or the LOS path, the recovered UWB signals are shown in Figure 7-6. In this diagram, the peak amplitude of each signal is normalized to one, and the waveforms are aligned so that this peak occurs at a common time sample. As can be seen from the figure, many of the normalized direct path waveforms have a similar shape, and in particular, a similar width from the peak to the first zero-crossing on either side. Recalling the recovered waveforms shown in Figure 6-12 through Figure 6-27, the waveforms which appear inverted may be from a propagation path which includes no walls, such as the measurements at location F2. These plots give an idea of what the characteristics of a filter matched to the direct path signal might need to be.

In a diversity or rake receiver, the goal is to consider more than one signal component. This implies that the characteristics of signals other than the direct path are also of interest. Defining the SNR as in equation 6.2, a detection threshold on the received signals is set at 12 dB below the SNR of the direct path signal at each measurement location. The lower envelope is defined as the smallest pulse width that might be encountered in a particular channel, and the upper envelope width is determined by the waveform with the largest extent in time that might be encountered in the channel. These numbers are determined by independently considering the upper and lower zero crossings on either side of the peak of the received signal waveform. In Figure 7-7, the ratio of the pulse with the largest support in time to the received waveform with the smallest support in time at each measurement location is plotted. There is a clear trend here in terms of the SNR of the LOS path at a particular measurement location. The larger the LOS SNR, the closer the ratio of the signal widths is to one, and the lower the SNR, the more this ratio tends to deviate from one. Two interpretations of this result can be put forth. First, the higher the SNR, the fewer the number of obstructions the pulse has experienced in propagating from the transmitter to the receiver. Thus fewer dispersion or distortion mechanism have perturbed the pulse, and the result is less variation in the shape of the received pulse. The second interpretation involves the detection threshold of 12 decibels below the SNR of the signal received on the direct path. In a high SNR case, a single signal with a large SNR might be received, followed by a rapid decay in the amplitude of the following signals. Thus the criterion is set relatively high, and a smaller percentage of the received signals exceed the detection threshold. In a smaller set of signals, less variation might be noted. Also shown in Figure 7-7 is a best fit line to the ratio of signal widths as a function of the SNR.

In Figure 7-8 through Figure 7-10, plots of the minimum and maximum time extent of the received signal waveforms at several different locations are shown.

7.3 UWB Channel Synthesis

In order to realize the practical significance of the channel models developed in this work, it is important to be able to apply them to the test and verification of ultra-wideband radio algorithms. Along these lines, the clustering model and the associated statistics for the cluster and ray arrival rates and angles from Chapter 6 are used to synthesize an UWB propagation channel. For this study, ideal second derivative Gaussian pulses are assumed; only the time and angle-of-arrival are accounted for. No attempt is made to model the distortions and dispersive

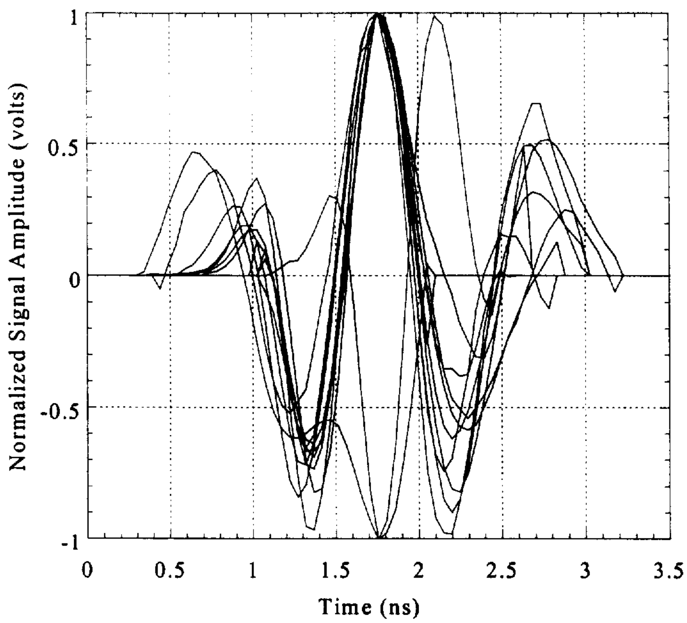

Figure 7-6: Received wavefroms from LOS path signals. Peak amplitude for each signal has been normalized to unity (recall recovered LOS signal at F2 for an example of the inverted pulse shape).

effects of the channel on a transmitted UWB pulse.

Some example scatter plots of the signal time-of-arrival and the angle-of-arrival information generated by the channel synthesis routine are shown below in Figure 7-11 - Figure 7-15. The signal arrival information shown in Figure 7-15 was also used to generate some examples of the synthesized received signal measurements. Two examples are given for different location in the measurement array. The first example is shown for two different time windows in Figure 7-16, and Figure 7-19 and the second example is shown in Figure 7-18 and Figure 7-19. These plots demonstrate, at least upon visual inspection, some consistency between the measured results and the recovered signal information and the synthesized signal information.

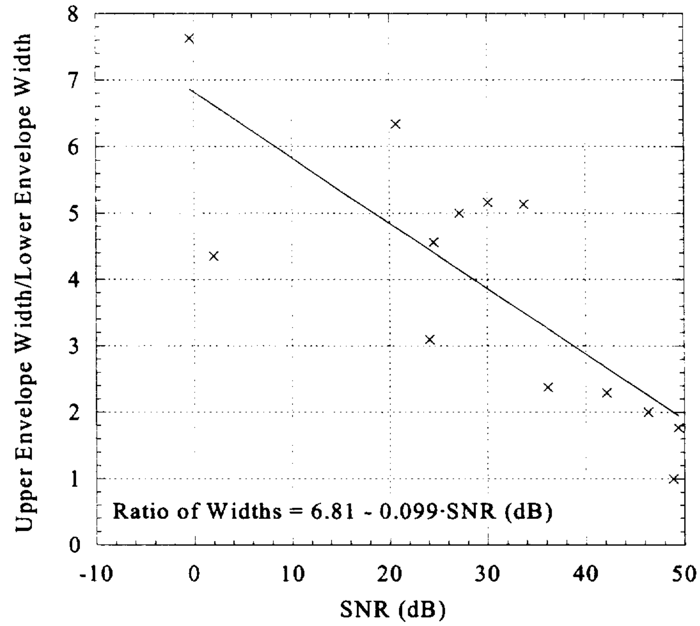

Figure 7-7: Ratio of the time extent of the upper envelope to the lower envelope vs. SNR. All signals within 12dB of the LOS path signal energy are considered.

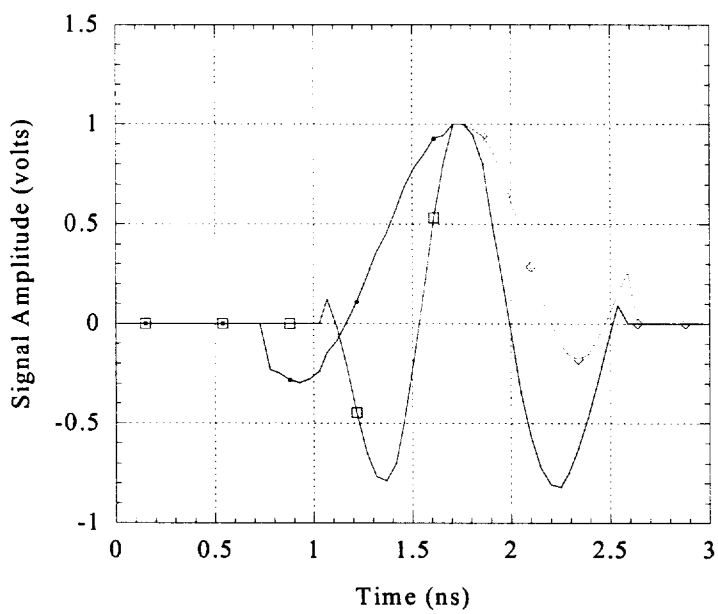

Figure 7-8: Upper and lower envelope of the received signal waveform at location P. All signals within 12dB of the strongest signal are considered.